 doi:10.20944/preprints202109.0459.v1

Investigation and Optimization of Mxene functionalized Mesoporous Titania Films as Efficient Photoelectrodes

Anum Iqbal[1] and Nasser M. Hamdan[2,*]

[1]Material science and Engineering Program

[2]Physics Department

The American University of Sharjah, Sharjah 26666, United Arab Emirates; [*]email: (nhamdan@aus.edu)

Abstract:

Three-Dimensional mesoporous TiO_2 scaffolds of anatase phase possess inherent eximious optical behavior that are beneficial in designing photoelectrodes for solar energy conversion applications. However, substantial efforts have been devoted in maximizing the UV and/or visible light absorption efficiency, and suppressing the annihilation of photogenerated charged species in pristine mesoporous TiO_2 structure for improved solar illumination conversion efficiencies. This study provides the fundamental insights into Mxene functionalized mesoporous TiO_2 as photoelectrode for the first time. This novel combination of Mxene functionalized TiO_2 electrodes with and without $TiCl_4$ treatments have been successfully optimized to intensify the process of photon absorption, charge segregation and photocurrent, resulting in superior photoelectrode performance. The photocurrent measurements of prepared photoelectrodes are significantly enhanced upon increased contents of Mxene due to improved absorption efficiency within the visible region as verified by UV–Vis absorption spectroscopy. Moreover, as evident through structural analysis, the anatase phase of TiO_2 is well grown due to increased contents of Mxene and post-deposition heat treatments. Consequently, an appreciable coverage of well-developed grains on FTO surface observed in SEM images. Thereby, the newly fabricated conductive mesoporous TiO_2 photoelectrodes are potential candidates for photoinduced energy conversion and storage purposes.

Keywords: Transition Metal Carbides, Power Conversion Efficiency (PCE), Surface Plasmon Resonance (SPR), Nano structuring, Photocatalyst, Mxene, Photoelectrodes, and Titania

Preprints (www.preprints.org) | NOT PEER-REVIEWED | Posted: 28 September 2021 doi:10.20944/preprints202109.0459.v1

Graphical Abstract

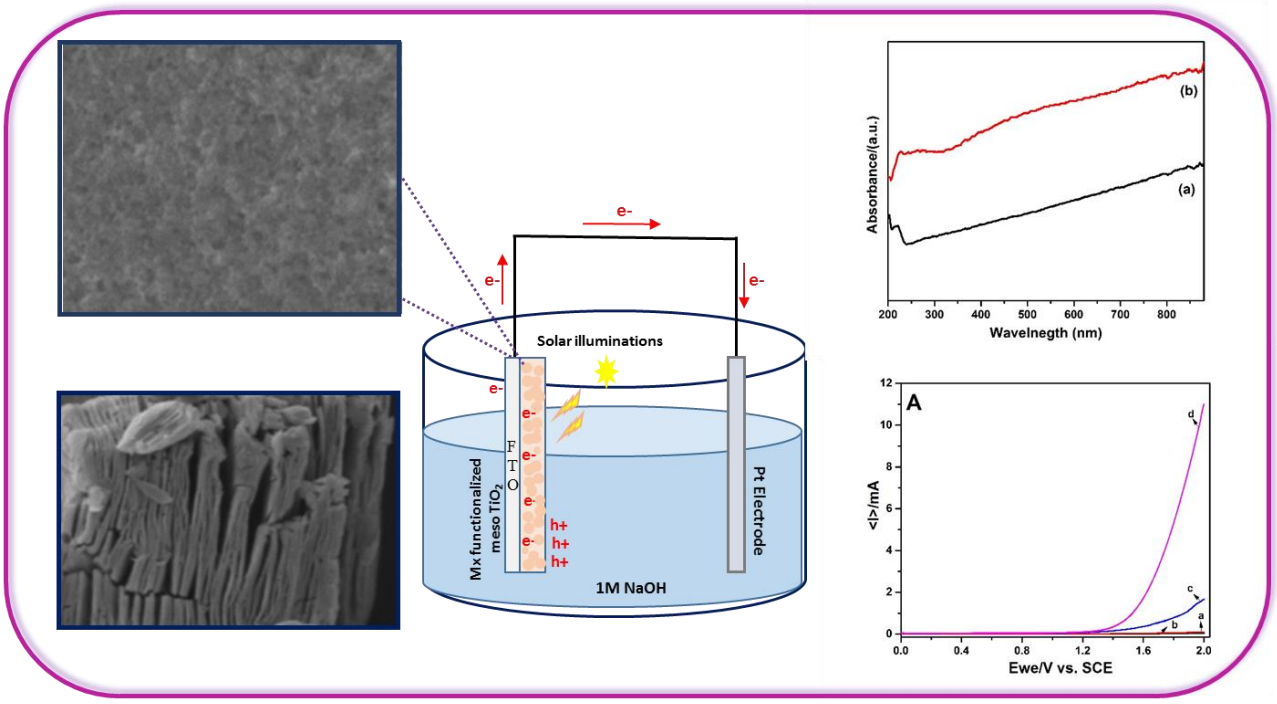

Highlights

- A novel Mxene functionalized Mesoporous TiO_2 photoelectrode with a strong interconnectivity between Mxene sheets and 3D mesoporous structure is developed.
- Improved optical and electrical properties of conductive anatase phase 3D TiO_2.
- Development of crack free films with Mxene modified $TiCl_4$ treatment.
- Mxene functionalized mesoporous TiO_2 is envisaged as a valuable platform for photoinduced energy conversion and storage applications.

 doi:10.20944/preprints202109.0459.v1

Introduction:

Solar radiations are the most significant source of a sustainable clean energy future. The practical utilization of solar radiations for generation of clean energy has been achieved through Photovoltaics and by mimicking photosynthesis in terms of photocatalysis [1]. The transformation of solar illuminations either into electric current or as energy carriers is broadly categorized into the domain of Photoelectrochemistry [2, 3]. The conversion efficacy of solar photons into charged species is mainly determined by charge separation efficiency as well as the quick charge conduction towards the electrode surface and are closely associated with the nanostructure and composition of a photoelectrode [4]. Therefore, constructing a photoelectrode capable of harvesting broad solar spectrum for required photovoltaic features has attracted the immense attention of researchers in material science. The typical process at a photoelectrode surface begins with the absorption of photons by a photoresponsive layer acting as a light absorber thus generating photogenerated charged species (e-/h+); followed by the rapid migration of these photogenerated charged species towards the electrode surface [5]. The photon absorption is strongly related to the inherent extinction coefficient and Nano structuring (band gap energy) which can be modulated to utilize a wide range of solar spectrum. Furthermore, the conversion efficiency of the absorbed photons and the kinetics of the photogenerated charges are greatly influenced by the recombining centers and conductance ability of photogenerated e^-/h^+ within the electrode nanostructure. The extended lifetime and smaller diffusion path for phototriggered charged species facilitate quick separation and rapid conductance of charges thus effectively improving the process conversion efficacies [6].

Thin films architecture is widely investigated as photoelectrodes in terms of composition, morphological features and structural attributes. These layered scaffolds possess several distinctive characteristics such as providing simplistic framework to anticipate and optimize the materials' essential features, particularly those associated with the dynamics of charged species in terms of their generation and charge transfer kinetics [7]. Consequently, thin film architecture exhibit effective substrate to study the basic aspects of solar energy harvesting materials. After analyzing the performance of a broad range of photoactive materials, it is inferred that a uni-compositional matrix fails to meet all the requirements of an effective conversion process that

Preprints (www.preprints.org) | NOT PEER-REVIEWED | Posted: 28 September 2021 doi:10.20944/preprints202109.0459.v1

includes photon assimilation, suppressed recombination rate, catalytic performance and passivation [8]. Therefore the development of a hybrid photoactive substrates composed of different chemical entities is a key approach to upgrade the efficiency of solar energy transformation reactions [9]. In these hybrid layered structures each entity serves a particular function such as the light active material that should have a modulated bandgap and electronic scaffold to maximize photon absorption of a suitable wavelength range. Furthermore, introducing co-catalysts on the top of the photoactive layer will minimize the (e-/h+) pair recombination process by facilitating quick charge separation due to close interaction between the layers. The ease of coating multiple layers of different composition on a single substratum makes the idea of hybrid film structure a more practical realm. Besides, various nanostructures of the electrode materials can also be developed to enhance the process efficiency by optimizing certain desired features [10].

A variety of synthetic methodologies for thin film fabrication have been introduced so far including Physical Vapor Deposition (PVD), Chemical vapor deposition (CVD), Atomic Layer deposition (ALD) and a few other techniques such as spin-coating and spray pyrolysis that are based on solution precursors [11]. These solution based techniques further strengthen the attributes of the fabricated films by enhancing the crystallinity and the strong chemical interaction between different chemical entities in a heterostructure due to post-growth annealing treatment [12]. Spin coating is the most widely inexpensive technique because of its design simplicity. The spin coating is comprised of four key phases [13]: (1) dispensing the precursor solution onto the substrate, (2) spin-up, (3) stable fluid out flow (spin off), and (4) Evaporation-induced drying (d). The thickness of the coated layer is mainly regulated by fluid flow in phase 3 and evaporation induced drying in phase 4. Most prominently, these two phases illustrate the co-occurrence of two processes (viscous flow and evaporation) throughout the coating procedures [14].

The highly desired characteristics (cost effectiveness, increased chemical firmness, environmental benign, and dominant photocatalytic attributes) of Titania TiO_2 for energy and environmental applications are well-known for decades [15]. Among various nanostructures, the anatase nanocrystalline mesoporous architectures of TiO_2 consisting of inter linked nanometric-sized spheres result in an increased surface area, large pore volumes, and tunable pore sizes with unique morphologies. Furthermore these morphological features also possess nanoscale effects in their

Preprints (www.preprints.org) | NOT PEER-REVIEWED | Posted: 28 September 2021 doi:10.20944/preprints202109.0459.v1

mesochannels as well as on their pore walls which are greatly desired for improved performance of energy devices [16]. The increased crystallinity with a fewer number of defects at peripheries without compromising the specific surface area is an effective strategy for decreased charge annihilation processes [17]. Moreover, the combined features of increased pore size and escalated surface area intensify the adsorption of surrounding molecules and kinetics of electrolytic species within the mesoporous TiO_2 framework thus enhancing the efficiency of Dye sensitized solar cells [18]. Likewise the efficiency of perovskite solar cells can be improved by regulating the crystallinity and growing stage of perovskite solution within mesoporous TiO_2 framework at increased annealing conditions [19]. The strong interaction of perovskite matrix with the mesochannels of TiO_2 supports the quick charge separation from the active layer thus and improving the PCE of the device [20].

Generally, the increased charge kinetics are favorable at thin pore walls and shorter mesochannels. [21]. Nevertheless, the conductance of photoinduced electrons within the oxide framework is supported by diffusion process and dominantly affected by the charge trapping and detrapping states due to crystallographic defects occurring within single particle and at contact peripheries among neighboring species [22]. Along with the influence of Nano confinement, the conductive mesoporous TiO_2 scaffolds have considerably reduced the hysteresis of IV curves in the forward and the reverse scanning directions. Since the addition of conductive species in mesoporous TiO_2 scaffolds reduces the presence of electronic trap sites thus enabling an enhanced electron conduction process [23]. Moreover the electron conduction within porous matrix has also been improved by fabricating porous one-dimensional (1D) architectures composed of TiO_2 films as photoanodes for improved PCE of perovskite based solar devices [24].

Up to now, a variety of materials including rare earth metals, metal oxides and carbonaceous substances has been used to dope and functionalize the pristine TiO_2 matrix. Among them, two-dimensional 2D carbonaceous substances like graphene have attracted immense consideration because of their unusual electrical conductance, and suppressed recombining effects of surface (e-/h+) pairs [25, 26]. Recently, the Transition metal carbides and nitrides, commonly called as MXenes, are newly emergent candidates among 2D materials. Typically, MXenes are derived from their corresponding MAX phase starting materials through the series of chemical events as shown

Preprints (www.preprints.org) | NOT PEER-REVIEWED | Posted: 28 September 2021 doi:10.20944/preprints202109.0459.v1

in the chemical equations 1-3, where M is the representative of transition metal (Sc, Ti, V, Cr, Zr, Nb, Mo,Hf, or Ta), A belongs to IIIA or IVA group, X could be C and/or N element [27].

$$M_{n+1}\,AX_n + 3HF \rightarrow AF_3 + {}^{3}/_{2}\,H_2 + M_{n+1}X_n \quad Eq\ 1$$

$$M_{n+1}X_n + 2H_2O \rightarrow M_{n+1}X_n(OH)_2 + H_2 \quad Eq\ 2$$

$$M_{n+1}X_n + 2HF \rightarrow M_{n+1}X_nF_2 + H_2 \quad Eq\ 3$$

So far, various MXenes composed of diverse transition elements have been studied including Ti_2CT_x,V_2CT_x, and Mo_2CT_x, where T signifies surface functional groups (-O, -OH, -F) [28, 29]. The distinct structural phase and attached surface functionalities induce unusual characteristics into Mxene scaffolds such as metallic conductivity, surface plasmon effects, hydrophilicity, greater surface area, and ability to anchor a broad range of intercalates [30-32]. So far, most MXenes are synthesized by etching Ti_3AlC_2 in HF acid due to low reduction potential of Al [33]. Since the Fermi band position of Ti_3C_2, O-functionalized Ti_3C_2, and F-functionalized Ti_3C_2 are -0.05, 1.88, and 0.15 V respectively relative to the Standard Hydrogen Electrode (SHE), locating at lower position than the conduction band minima of TiO_2 [34]. Therefore, the relative location of the bands in $Ti_3C_2T_x$ manifest appreciable transfer of photogenerated electrons from TiO_2 matrix to Mxene thus reducing the chances of (e^-/h^+) annihilation [35].

Herein, TiO_2 scaffolds are functionalized with Ti_3C_2 Mxene (Mx) sheets within each spin coated layer in three different steps. For the first TiO_2:Mx layer, Mxene dispersion with fixed volume has been added in TiO_2 solution and then spin coated on FTO substrates through two step spin coating procedure. The effects of subsequent $TiCl_4$ treatment are intensified by immersing the fabricated TiO_2:Mx films in $TiCl_4$:Mx (with varying amounts of Mxene) solution. Finally the fabrication of the desired photoelectrodes is accomplished by depositing Mesoporous Titania paste with and without Mxene through special annealing under ramping conditions. Therefore, this study is the foremost attempt in providing basic insights into Mxene functionalized mesoporous Titania photoelectrodes of anatase phase with improved photovoltaic features.

Preprints (www.preprints.org) | NOT PEER-REVIEWED | Posted: 28 September 2021 doi:10.20944/preprints202109.0459.v1

Experimental Section

Materials and Methods

Titanium Aluminum carbide Ti_3AlC_2 powder (> 98 wt% purity), Hydrofluoric acid HF solution (40 wt.%), Fluorine-doped tin oxide (FTO, 7 Ω square-1) glass, Acetone, Ethanol, Titanium disopropoxide bis (Acetylacetonate), Titanium Tetra chloride solution $TiCl_4$, Mesoporous TiO_2 commercial paste were of analytical grade. All these chemicals were purchased from Sigma Aldrich. De-ionized water was utilized throughout the experimental scheme.

Synthesis of Mxene (Ti_3CT_x) Powder

MXene was prepared through a conventional method based upon selective etching of Ti_3AlC_2 powder in HF solution [36-40]. Commercial Ti_3AlC_2 powder (> 98 wt% purity) was used without further purification. In a typical synthesis, 3.0 g of Ti_3AlC_2 powder was dissolved in HF solution (40 wt.%, 50 mL). For this purpose, the HF was first poured in plastic beaker placed in an ice bath. Once HF solution cools down below room temperature, the desired amount of Ti_3AlC_2 was slowly added to the HF solution with continuous stirring. After the complete addition of Ti_3AlC_2 within 90 minutes, the solution was stirred under the same ice condition for an additional 30 minutes. Subsequently, the solution was subjected to sonication for 2 hours. During sonication the ice water bath was refreshed after every 13 minutes. Lastly, for successful etching of Al layers the solution was kept at room temperature while stirring for 24 h. Then the slurry was separated from HF liquid media through centrifugation at 3500rpm for 15 minutes. After decanting the supernatant, the sediment was repeatedly washed with DI water by progressively increasing the centrifugation speed up to 6000rpm. When the pH reaches closer to the desired value of 7, the sediment becomes more water soluble (an indication of the successful etching of Ti_3AlC_2 powder). Therefore, in the present study the centrifugation time was increased up to 45 minutes at 7000rpm for each cycle. The thoroughly washed slurry was then subjected to vacuum filtration. Finally, the Mxene powder was achieved through drying the vacuum filtered cake at room temperature for further characterization. The pictorial representation of each step is presented in fig1.

Preprints (www.preprints.org) | NOT PEER-REVIEWED | Posted: 28 September 2021 doi:10.20944/preprints202109.0459.v1

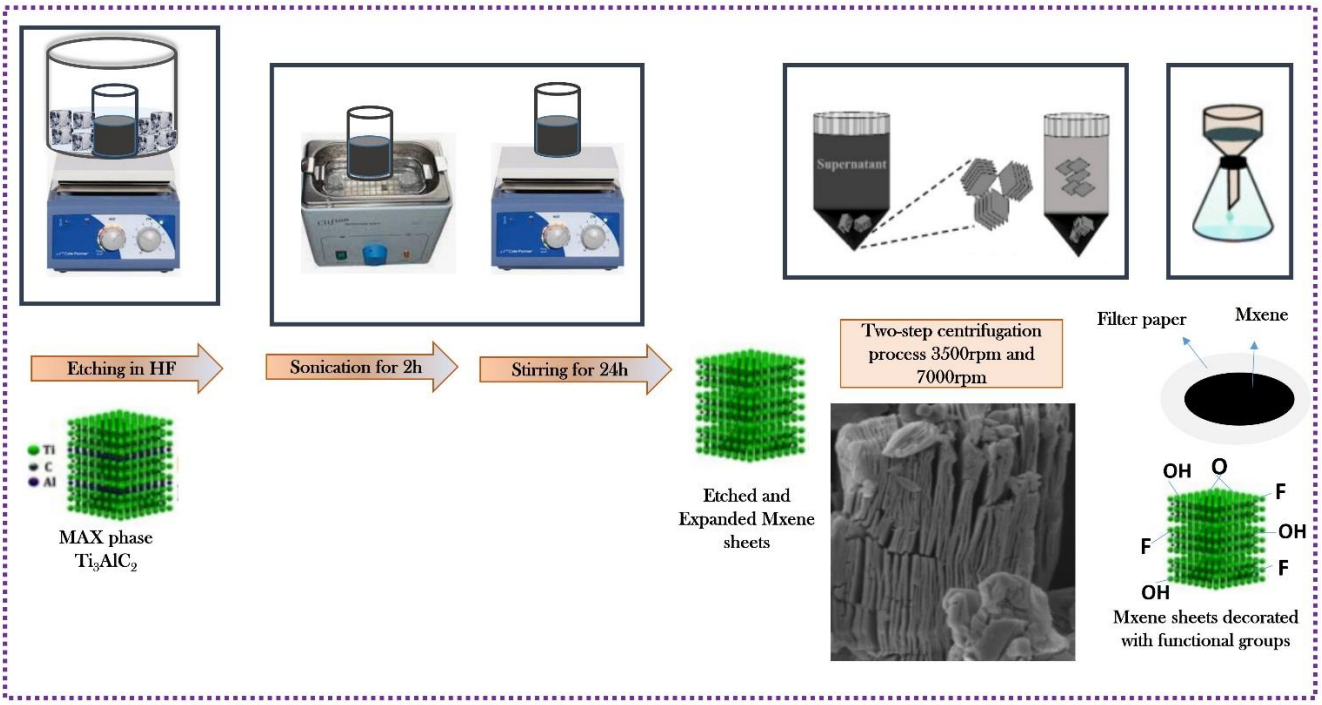

Figure 1: Schematic representation of stages involved in the synthesis of Mxene sheets

Fabrication of TiO_2:Mxene Films

(a) Steps for Spin Coating: Fluorine-doped tin oxide (FTO, 7 Ω square^{-1}) glass substrates with dimensions of 2cm x1.5 cm were gently cut through a glass cutter. The FTO substrates with the required dimensions were cleaned sequentially in sonication bath by utilizing detergent solution, deionized water, acetone, and ethanol for 30 minutes each and blow-drying with air stream. Substrates were then treated by UV-O_3 for 40 minutes to remove any organic contaminants. Fig. 2 represents the stages involved in the fabrication of Mxene modified Mesoporous Titania Photoelectrodes. A thin compact TiO_2:Mxene scaffold was spin coated on the required FTO sizes through two step process: (1) spinning at 4000rpm for 20s just after dropping down the required solution and then followed by (2) immediate drying at 8000rpm for 10s. Since high spinning speed results in thinning of the layer with uniform evaporation of the solvent. The chemical entities of high volatility in deposited solution can be removed from the substrate through high spinning speed, but the compounds of low volatility remain on the surface of the substrate [41]. Therefore the coated films were further dried at 120^{o}C for 5 minutes on a hotplate. The dried films were then

Preprints (www.preprints.org) | NOT PEER-REVIEWED | Posted: 28 September 2021 doi:10.20944/preprints202109.0459.v1

annealed at 500ºC for 30minutes in ambient air. The as prepared films were then subjected to Mxene modified and simple $TiCl_4$ treatment respectively.

(b) Preparation of Mxene:TiO_2 precursor solution The precursor solution for TiO_2:Mxene films was prepared by adding 0.586 ml of Mxene dispersion (0.5mg/ml in ethanol) and 0.586 ml of titanium disopropoxide bis (acetylacetonate) (99.9% Sigma-Aldrich) in 3.414ml of ethanol. The prepared solution was stirred for 10 minutes before depositing on FTO substrates. Then 110µl of this solution was dropped onto the FTO substrates.

(c) Mxene modified $TiCl_4$ treatment: The TiO_2:Mx films were then subjected to $TiCl_4$ treatment with or without Mxene. The coated TiO_2 films were immersed into 40 mM $TiCl_4$ aqueous solution at 70 °C for 60 min in a pre-heated drying chamber. The FTOs were then washed vigorously with DI water and ethanol as well as blow dried with air stream. Finally post heat conditions were set at 500 °C for 1hr. However in Mxene modified $TiCl_4$ treatment, with varying amounts of Mxenes (0.25 mg/ml and 0.37 mg/ml of Mxene) were added to the $TiCl_4$ aqueous solution respectively under the same processing condition.

(d) Deposition of Mxene modified Mesoporous layer: In each aforementioned scaffold the mesoporous TiO_2 layer was deposited through spin-coating by diluting the commercial paste (30-TS, G24 Power Ltd., 30-TS/ethanol = 1/7, w/w) in ethanol at 6000 rpm for 25s. Finally, the meso layer was annealed under ambient condition through the following ramping heat treatment: 325 °C for 15 min, 375 °C for 10 min, 450 °C for 10 min, 500 °C for 5 min. However, the conductive mesoporous Titania scaffold was achieved by adding a fixed amount of Mxene in ethanol solution which was used to dilute the meso Titania paste. The varying compositions of all the prepared photoelectrodes with their labeling are presented in table 1.

Preprints (www.preprints.org) | NOT PEER-REVIEWED | Posted: 28 September 2021 doi:10.20944/preprints202109.0459.v1

Table 1. A list of varying compositions in all prepared photoelectrodes.

No of Samples	Photoelectrode Architecture	Photoelectrode Labelling
1	Glass/FTO/TiO_2:Mx	Sample A
2	Glass/FTO/TiO_2:Mx/$TiCl_4$	Sample B
3	Glass/FTO/TiO_2:Mx/$TiCl_4$:0.25 Mx	Sample C
4	Glass/FTO/TiO_2:Mx/$TiCl_4$:0.37 Mx	Sample D
5	Glass/FTO/TiO_2:Mx/mTiO_2	Sample E
6	Glass/FTO/TiO_2:Mx/$TiCl_4$:mTiO_2	Sample F
7	Glass/FTO/TiO_2:Mx/$TiCl_4$:0.25 Mx/mTiO_2	Sample G
8	Glass/FTO/TiO_2:Mx/$TiCl_4$:0.37 Mx/mTiO_2	Sample H
9	Glass/FTO/TiO_2:Mx/mTiO_2+Mx	Sample I
10	Glass/FTO/TiO_2:Mx/$TiCl_4$/mTiO_2+Mx	Sample J
11	Glass/FTO/TiO_2:Mx/$TiCl_4$:0.25Mx/mTiO_2+Mx	Sample K
12	Glass/FTO/TiO_2:Mx/$TiCl_4$:0.37Mx/mTiO_2+Mx	Sample L

Preprints (www.preprints.org) | NOT PEER-REVIEWED | Posted: 28 September 2021 doi:10.20944/preprints202109.0459.v1

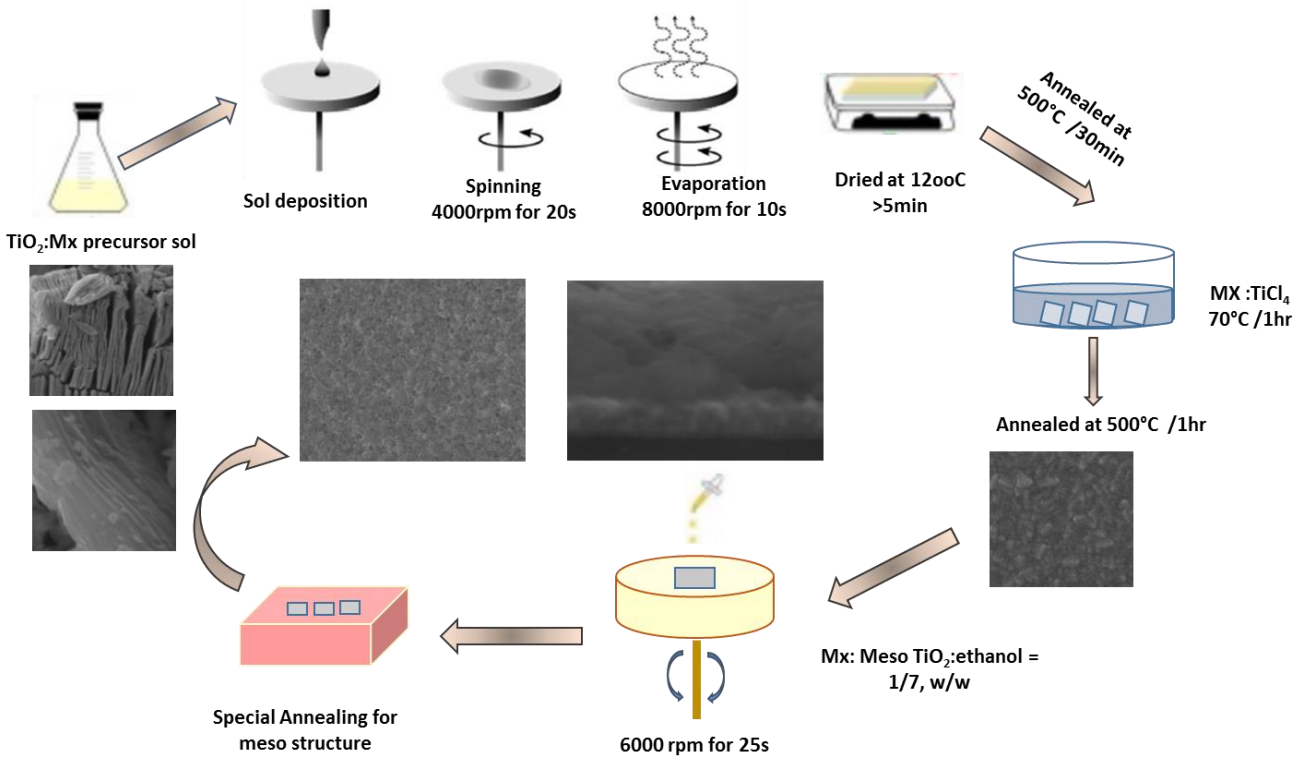

Figure 2. Stages involved in the fabrication of Mxene modified Mesoporous Titania Photoelectrodes.

Materials Characterization

The crystallographic study of synthesized samples has been done through X-Ray Diffraction (XRD) technique using a Bruker D8 ADVANCE system with a Cu tube source and a linear detector (LYNXEYE XE). The Raman spectrum have been recorded on a Raman spectrometer (JYHR800, Horiba Jobin Yvon, France) using 514.5 nm laser excitation. A TESCAN environmental scanning electron microscope (VEGA3 XMU) with a LaB_6 source and Oxford Aztec X-Max 50 EDS are used for imaging and elemental mapping of the materials. The optical features of all prepared samples have been studied through UV-Vis spectrophotometer UV-2600i Shimadzu corp. Current-Voltage measurements were performed through an electrochemical workstation (Keithley, 2420 Source Meter) under solar illumination (100 mW cm^{-2}) calibrated by a standard silicon solar cell (Oriel Instrument).

Mxene Powder Characterization

Structural Analysis

Preprints (www.preprints.org) | NOT PEER-REVIEWED | Posted: 28 September 2021 doi:10.20944/preprints202109.0459.v1

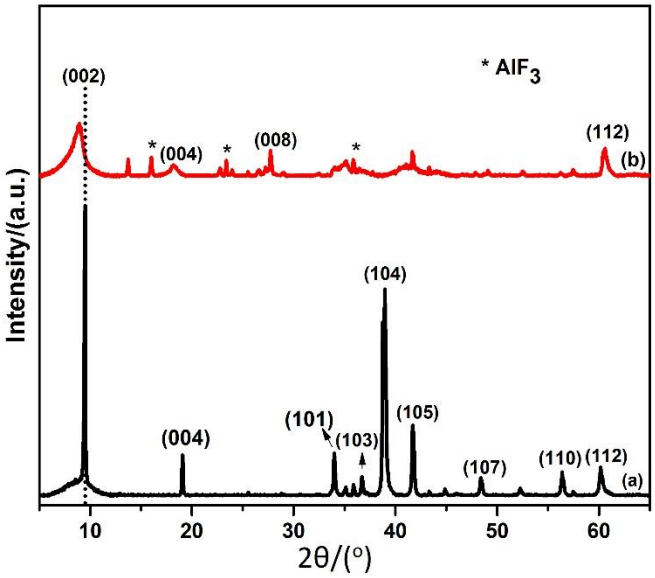

Figure 3: (A) XRD patterns of Ti_3AlC_2 MAX precursor (a) and as-synthesized $Ti_3C_2T_x$ Mxene (b).

The Fig. 3 (A) presents XRD patterns of Ti_3AlC_2 MAX powder used as starting material (a) and etched $Ti_3C_2T_x$ Mxene (b) in HF acidic solution. The strong diffraction peaks of the starting material Ti_3AlC_2 are observed at $2\theta = 9.5^o$, 19.0^o, 34.0^o, 36.7^o, 38.9^o, 41.7^o, 48.3^o, 56.4^o, and 60.1^o [42, 43]. In a broader context and due to selective etching of Al layers from the starting material in HF assisted exfoliation process, the peaks are considerably shifted to lower angles (8.8^o, and 18.2^o) in XRD spectrum of synthesized $Ti_3C_2T_x$ MXene. This shift suggests the increased d spacing in synthesized $Ti_3C_2T_x$ MXene (as found in SEM images below) compared to the starting Ti_3AlC_2 MAX phase. The increase in d spacing is due to structural expansion from etching and considerable substitution of Al with –F and –OH/=O terminating groups [44-46]. Moreover, the broadness and suppressed intensity of peaks in XRD pattern of $Ti_3C_2T_x$ MXene indicate less crystallinity and perturbed structural order of sheets which supports the successful treatment in HF acidic solution [47]. Along with these observations, the most intense peak at $2\theta=38.9°$ nearly disappeared in $Ti_3C_2T_x$ MXene, confirming the substantial removal of Al layers from Ti_3AlC_2 [48]. Furthermore, a new peak at 27.7^o (008) is noticed which is due to the formation of $Ti_3C_2(OH)_2$ in agreement with the Li et al [49]. Besides, the appearance of other less intense peaks (marked with *) are attributed to the residuals of Al element in $Ti_3C_2T_x$ which is difficult to be removed completely within 24 hours of soaking time leading the formation of AlF_3 [50-52]. These results suggest the $Ti_3C_2T_x$ surfaces are decorated with functional entities of -O, and -F after HF treatment as supported by EDS spectra [53, 54].

Preprints (www.preprints.org) | NOT PEER-REVIEWED | Posted: 28 September 2021 doi:10.20944/preprints202109.0459.v1

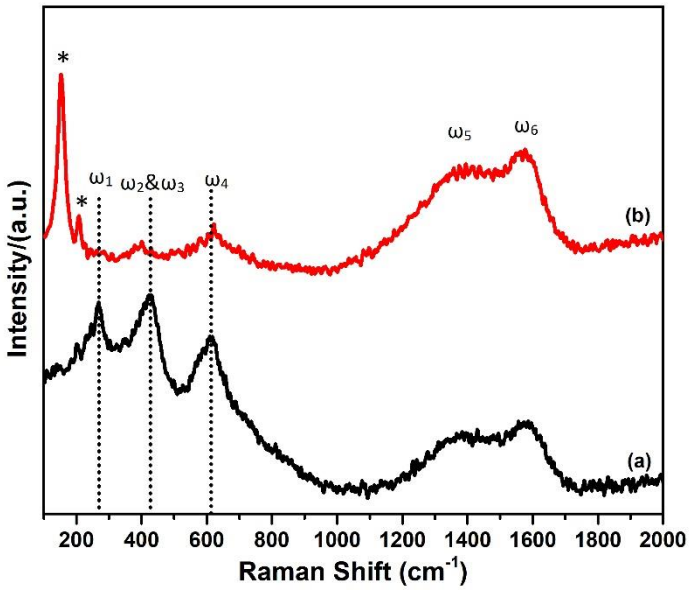

Figure 4. Raman Spectra of Ti_3AlC_2 MAX powder (a) and $Ti_3C_2T_x$ Mxene (b).

Fig 4 shows Raman spectra for Ti_3AlC_2 starting material MAX phase (a) and etched $Ti_3C_2T_x$ Mxene (b). The peaks labelled as ω_1, ω_2 & ω_3, ω_4 in spectrum (a) are located around 269, 423, and 613 cm^{-1} respectively. These peaks, are key features of Ti_3AlC_2 and well-matched with the reported literature assigning towards the shear and longitudinal oscillations of Ti and the Al atoms [55-58]. Specifically, ω_1 is associated with vibrations of the Al, and its disappearance in spectrum (b) correlates with the substantial etching of Al atoms resulting into Mxene structure [59]. The broadening of the peaks in spectrum (b) corresponds with decrease in order as expected by the exfoliation process and was also observed in the XRD spectrum discussed above [60]. Additionally, another two broad peaks are observed in the range of 1000-1800 cm^{-1}. These two broad peaks are assigned to the D and G peak of graphitic carbon signifying the presence of carbon and disorder in the samples [61]. The increased intensity of these two peaks shows that the surfaces are exposed to more carbon. The graphitic carbon can greatly enhance the charge transfer character of the carbide layer which is highly advantageous for the improved Photoconversion efficiencies of energy devices [62]. Both G and D peaks are due to sp^2 sites. However, the occurrence of G-band links with the stretched C-C bond in carbonaceous substances and is commonly associated with all sp^2 rings and chains architectures [63]. Contrary to it, D peak occurs only in perturbed sp^2 rings [64]. It is worth noting the peak at 208 (explicitly marked with *) involve out-of plane vibrations of Ti and C atoms [51, 65-68]. More prominently, there is an intense peak at around 151 cm^{-1}. The high intensity of this peak could be related to the increased laser power, leading to the

Preprints (www.preprints.org) | NOT PEER-REVIEWED | Posted: 28 September 2021 doi:10.20944/preprints202109.0459.v1

formation of oxidized Ti_3C_2 [54, 69]. All these facts are well supported by various literature and signify successful synthesis of $Ti_3C_2T_x$.

Optical Features

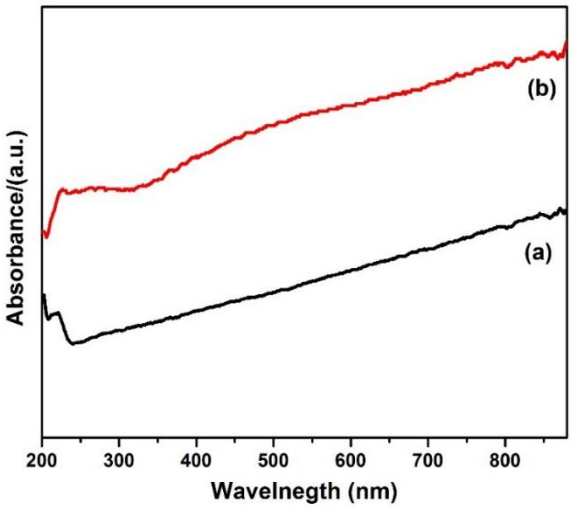

Figure 5. UV-Vis spectra of Ti_3AlC_2 MAX precursor (a) and $Ti_3C_2T_x$ Mxene (b).

The optical-response of Ti_3AlC_2 MAX precursor and as-synthesized Mxene powder is investigated through the ultraviolet-visible (UV-Vis) absorption spectra. The Ti_3AlC_2 (curve a) fig 5 and pristine $Ti_3C_2T_x$ (curve b in fig 5) display good optical response for the incident light range of 200–800 nm due to the black color of Ti_3C_2 with no clear absorption edge, indicating the metallic nature of Ti_3C_2 [70-73]. The broadness of these UV-Vis absorption bands are well-correlated with the previously reported optical features of MXenes and referred to the localized surface plasmon resonance (LSPR) effect [74-77]. Surface plasmonic resonance effects (SP) are surface electronic oscillations existing at an inter linked boundary of metal with dielectric material [78, 79]. Moreover, the surface effects become more pronounced with the increased interlayer distance among underlying Mxene sheets. Therefore the absorption intensity of Mxene in curve b increases significantly in comparison of Ti_3AlC_2 precursor phase [80-82].

Preprints (www.preprints.org) | NOT PEER-REVIEWED | Posted: 28 September 2021 doi:10.20944/preprints202109.0459.v1

Morphological and compositional Analysis

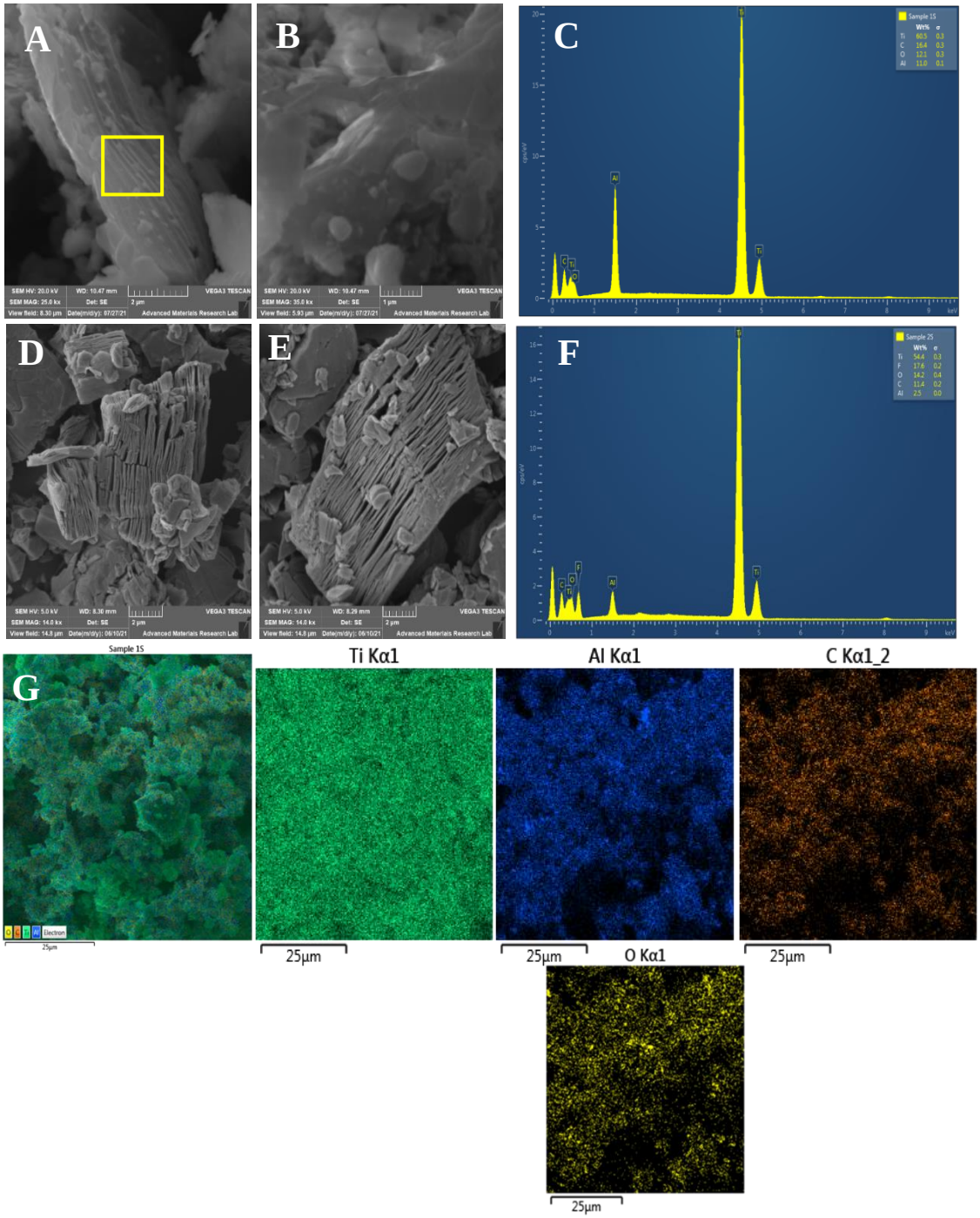

Preprints (www.preprints.org) | NOT PEER-REVIEWED | Posted: 28 September 2021 doi:10.20944/preprints202109.0459.v1

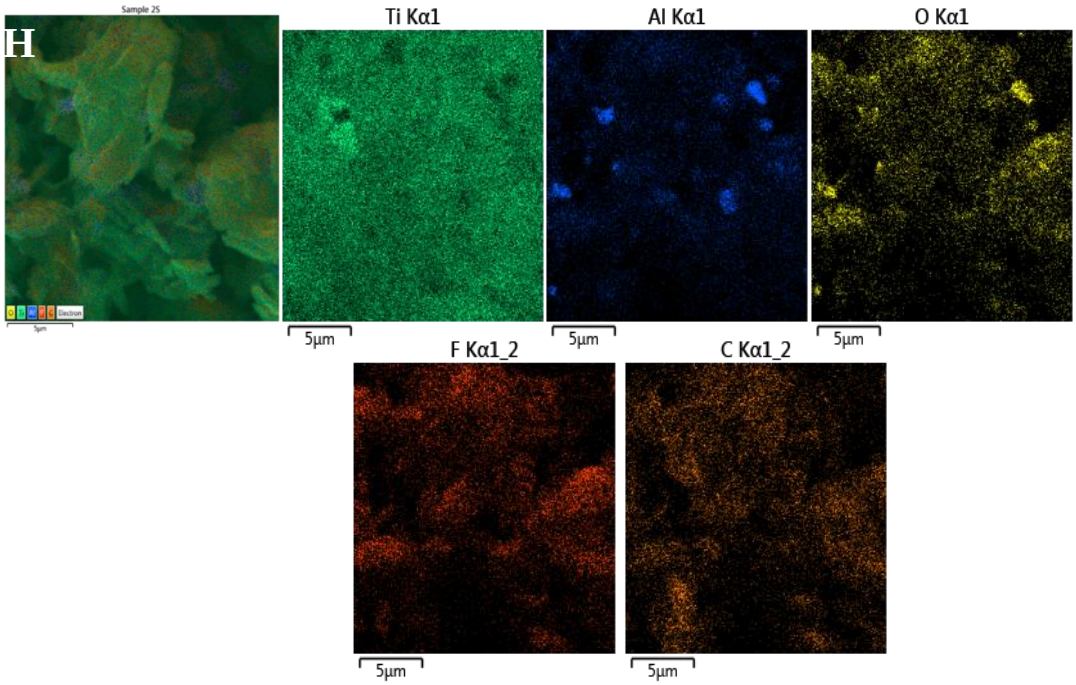

Figure 6. (A) SEM image of the side view of Ti_3AlC_2 sheets; (B) SEM image of Ti_3AlC_2 sheets in the top view; (C) EDS spectra of Ti_3AlC_2 MAX phase powder; (D,E) an SEM image of $Ti_3C_2T_x$ in the side view; (F) EDS spectra of $Ti_3C_2T_x$ Mxene; (G) Color EDS mapping of Ti_3AlC_2 ; and (H) Color EDS mapping of $Ti_3C_2T_x$ Mxene.

SEM images provide the visual interpretation of surface morphological features for synthesized materials. Fig 6A shows the side view of Ti_3AlC_2 sheets, indicating the close-packed layer structure marked with a square box. Likewise, fig 6B exhibits a typical top view of Ti_3AlC_2 precursor, with the lateral dimensions around 4 µm. The EDS spectra (fig 6C) and colorful maps (fig 6G) of Ti_3AlC_2 precursor show the contents of Ti, C and Al elements indicating good purity level of the utilized Ti_3AlC_2 MAX phase as precursor. Fig 6D shows well-spaced and parallel layer in Mxene sheets because of HF acidic treatment. The resulting Ti_3C_2 has an interspacing of 0.38µm, which is more than that found in bulk Ti_3AlC_2 (~0.16 µm). Such morphological transformations are similar to those observed in the literature [83] indicating the effective removal of Al layers from the precursor matrix. Figure 6E shows a few small spherical particulates with diameter about ~0.53 µm, and tiny sheet-like fragments of lateral dimensions 1.49 µm attached to the layered edges of Ti_3C_2. These small spherical species are considered as AlF_3 byproducts formed during the etching of Ti_3AlC_2 with HF [84] supported by the presence of Fluorine and small contents of Al in EDS spectra of synthesize $Ti_3C_2T_x$ Mxene (fig 6F). Due to etching of Ti_3AlC_2 in HF, the newly produced layered scaffold could be highly unstable because of increased surface energy. Thence, while minimizing the surface energy the resultant layered structure got

Preprints (www.preprints.org) | NOT PEER-REVIEWED | Posted: 28 September 2021 doi:10.20944/preprints202109.0459.v1

stabilized by anchoring the small fragments of Ti_3C_2 [85]. Therefore, after etching of Ti_3AlC_2 with HF in a controlled environment the exfoliated, and lamellar Ti_3C_2 is successfully produced with Ti, C, O and F as the main components indicated in fig 6H whereas the amount of Al element is considerably decreased as compared to that found in Ti_3AlC_2 MAX phase precursor.

Film Characterization

UV-Vis Absorbance Spectroscopy

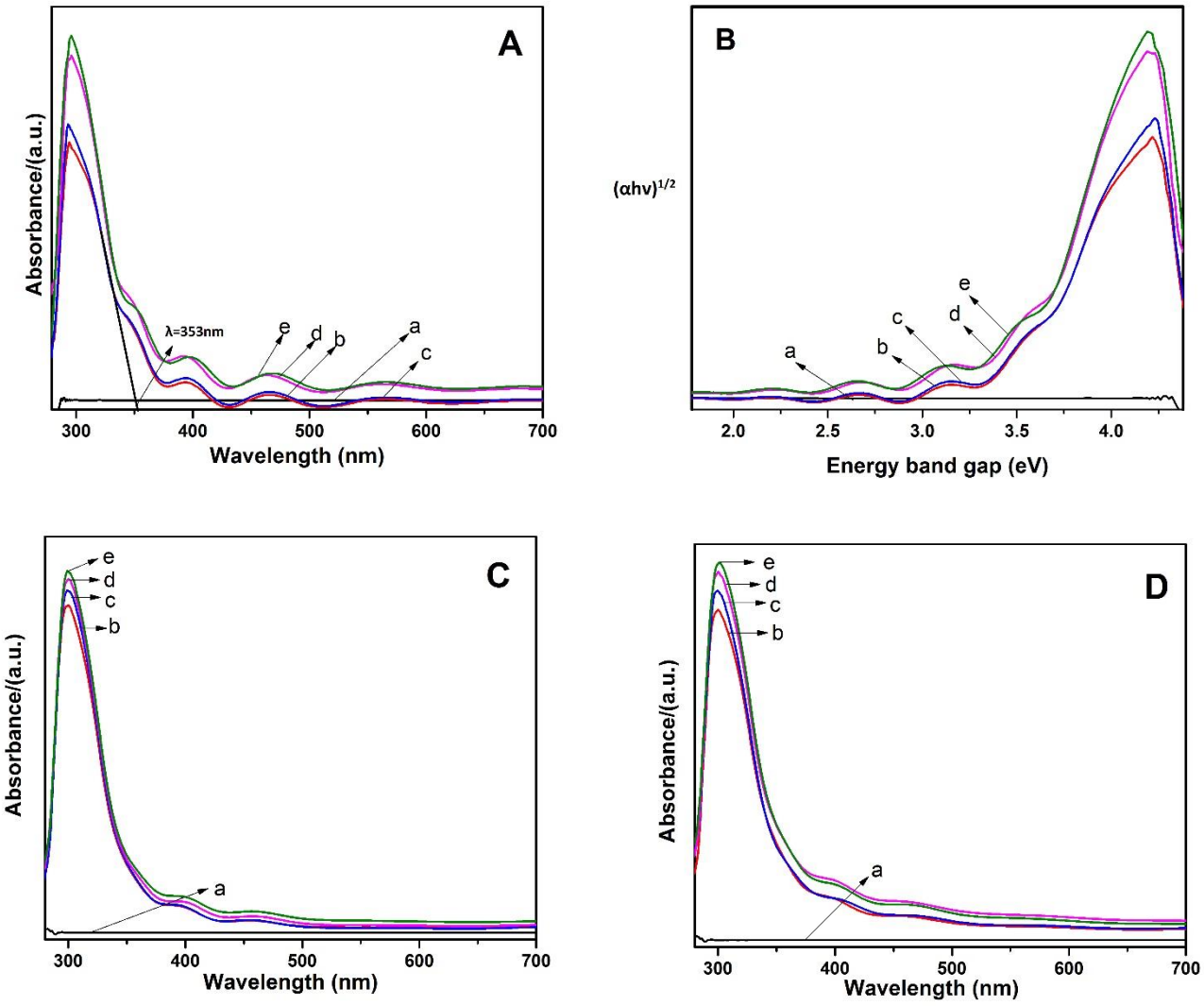

Preprints (www.preprints.org) | NOT PEER-REVIEWED | Posted: 28 September 2021 doi:10.20944/preprints202109.0459.v1

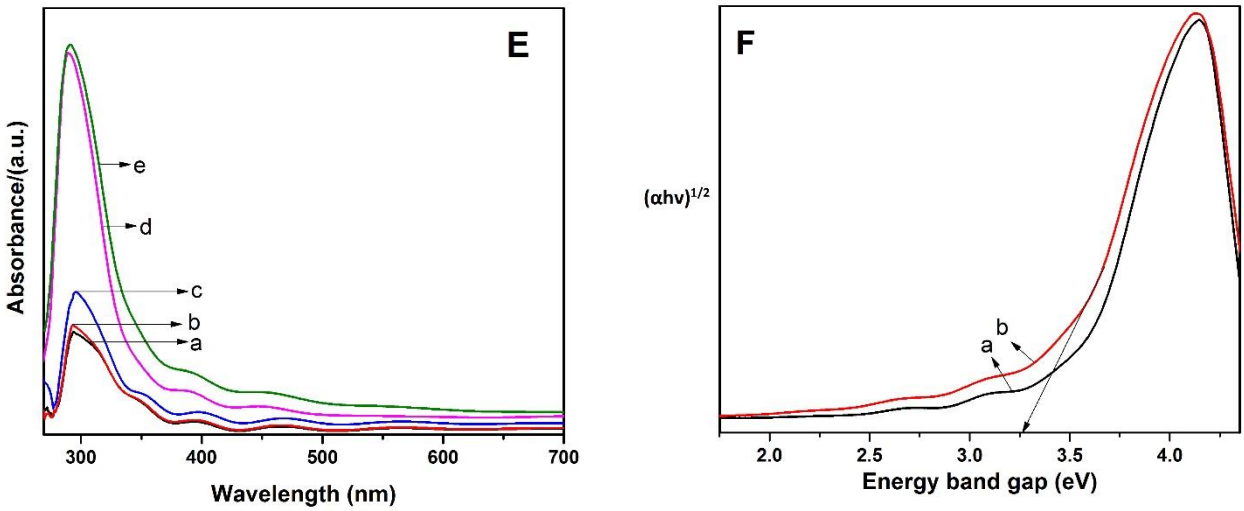

Figure 7. UV-Vis absorption Spectra (A) and tauc plot for corresponding Energy band gap values (B) for Group 1 composed of (a) Bare FTO, (b) Sample A, (c) Sample B, (d) Sample C, and (e) Sample D. UV-Vis absorption Spectrum (C) for Group 2 composed of (a) Bare FTO, (b) Sample E, (c) Sample F; (d) Sample G; and (e) Sample H and UV-Vis absorption Spectrum (D) Group 3 composed of (a) Bare FTO, (b) Sample I; (c) Sample J(d) Sample K and (e) Sample L. (E) An overview of UV-Vis absorbance behavior of (a) Sample A; (b) Sample B (c) Sample D, and (d) Sample H; (e) Sample L (F) Tauc plot for corresponding Energy band gap values of (d) Sample H; (e) Sample L.

The optical behavior of all the coated films on FTO substrates has been characterized using UV-Vis spectroscopy as displayed in fig 7. All the samples display good light-absorbing feature in the range of 350–700 nm which leads to enhancement of the Opto-electronic device performance [86, 87]. The main TiO_2 absorption peak at wavelength less than 350 nm is clearly observed in all prepared film spectra which is consistent with the published data [88-90]. Fig 7A shows a slight increase in the absorption intensity due to $TiCl_4$ treatment. On the other hand, a prominent increase in absorption intensity is observed due to addition of Mxene in conventional $TiCl_4$ treatment due to unique intrinsic optical features of Ti_3C_2 nanosheets presented in fig 5. Such increased UV-Vis absorption behavior became more pronounced upon increasing the Mxene content. The improved optical response is also related to good film uniformity, and dense coverage on the FTO substrates as supported by XRD analysis [91]. Similarly, with mesoporous Titania tremendous increase in the absorption peak intensity has been observed for all samples as shown in fig 7C. Moreover, a

Preprints (www.preprints.org) | NOT PEER-REVIEWED | Posted: 28 September 2021 doi:10.20944/preprints202109.0459.v1

significant increase in the absorption behavior within the visible region was observed (Fig 7D) in the case of Mxene functionalized mesoporous Titania. A clear difference in the photon absorption intensity due to mesoporous layer deposition is prominently visible in fig 7E. The figure also shows a pronounced increase in light absorption efficiency within the visible region as shown in the green curve due to Mxene addition in the finally deposited Mesoporous layer.

Band alignment and band gap are another important characteristics that describes the optical features of photocathode. The energy band gap values of all prepared films are determined through Tauc's method given in Eq 4 [92].

$$(\alpha hv)^n = A\left(hv - E_g\right) \qquad Eq4$$

where A is a constant, and Eg is the band gap energy and n is a number specifying the transition process. The value n=2 is assigned for a direct transition and ½ for an indirect transition [93]. The most widely used methodology to determine Eg involves plotting $(\alpha hv)^n$ against photon energy hv. The plot of $(\alpha hv)^{1/2}$ versus photon energy (hv) is shown in fig. 7B and 7F. The calculated energy band gap value of TiO_2:Mxene film is 3.51 eV fig 7b which is then downshifted to 3.44 eV in Mxene modified $TiCl_4$ treated TiO_2:Mxene. Moreover, further reduction in energy band gap down to 3.26eV has been found in Mxene functionalized Mesoporous Titania layer (Fig 7F) due to larger contents of Mxene. The improvements in the optical and electronic properties of Mxene functionalized Mesoporous Titania are in agreement with the obtained IV characteristics of films shown below.

Structure analysis of the Mxene functionalized Mesoporous Titania layer

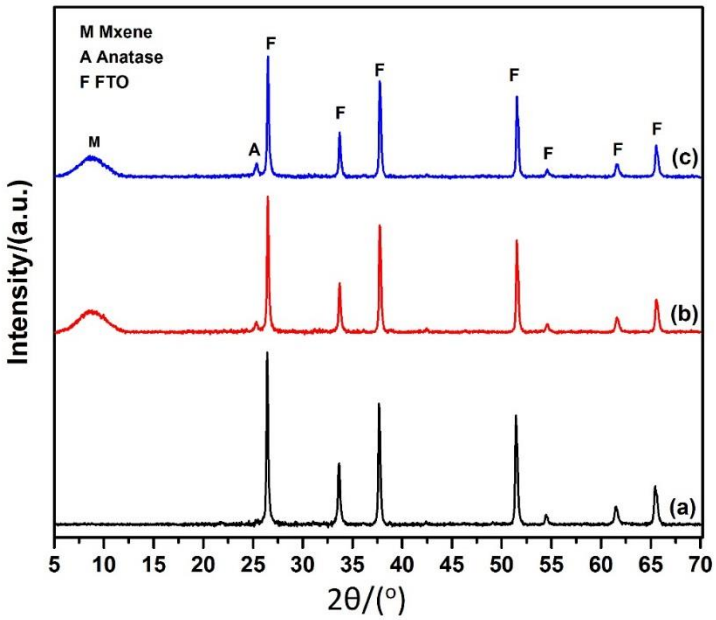

Preprints (www.preprints.org) | NOT PEER-REVIEWED | Posted: 28 September 2021 doi:10.20944/preprints202109.0459.v1

Figure 8. XRD spectra of (a) bare FTO, (b) Sample H, (c) Sample L.

The structural, phase identification and crystallinity of the deposited films are investigated by XRD. Fig 8 shows the XRD patterns of FTO substrate (a);Sample H: Glass/FTO/cTiO$_2$+Mx/TiCl$_4$+3%Mx/mTiO$_2$(b),SampleL:Glass/FTO/cTiO$_2$+Mx/TiCl$_4$+3%Mx/m TiO$_2$+Mx (c). The figure demonstrate that the fabricated films are composed of tiny single anatase peak of TiO$_2$ (101) phase at 2θ=25.2^o and a broad peak at 2θ=8.6^o (002) for Mxene. The peaks positions for both Mxene and Anatase phase are in agreement with the reported literature [94-97]. For comparison purpose, XRD pattern of the (a) bare FTO is also shown in fig 8 composed of several peaks indexed at 2θ= 26.49^o, 33.6^o, 37.69^o, 51.48^o, 61.44^o, and 65.48^o with identified planes are (110), (101), (200), (220), (221), and (301) respectively [98]. Interestingly, due to Mxene contents in TiCl$_4$ treatment and Mesoporous layer the peak of TiO$_2$ has become more prominent supporting the increased crystallinity and well-grown Anatase phase of TiO$_2$. The heat treatment of Mxene in open air at high temperature reinforces the formation of Anatase phase [99]. Besides, the characteristic peaks of FTO substrate have been suppressed considerably in as-prepared films. The anatase phase of TiO$_2$ is reported for providing better electron conduction with greater absorption coefficient [100]. The improved crystallinity in the films is advantageous for achieving superior photoelectric conversion activities. Since, well developed crystalline attributes assure enhanced photo stability for efficient conduction of phototriggered charge carriers [101]. These factors enhance the photo assisted electrical conductance of the fabricated films.

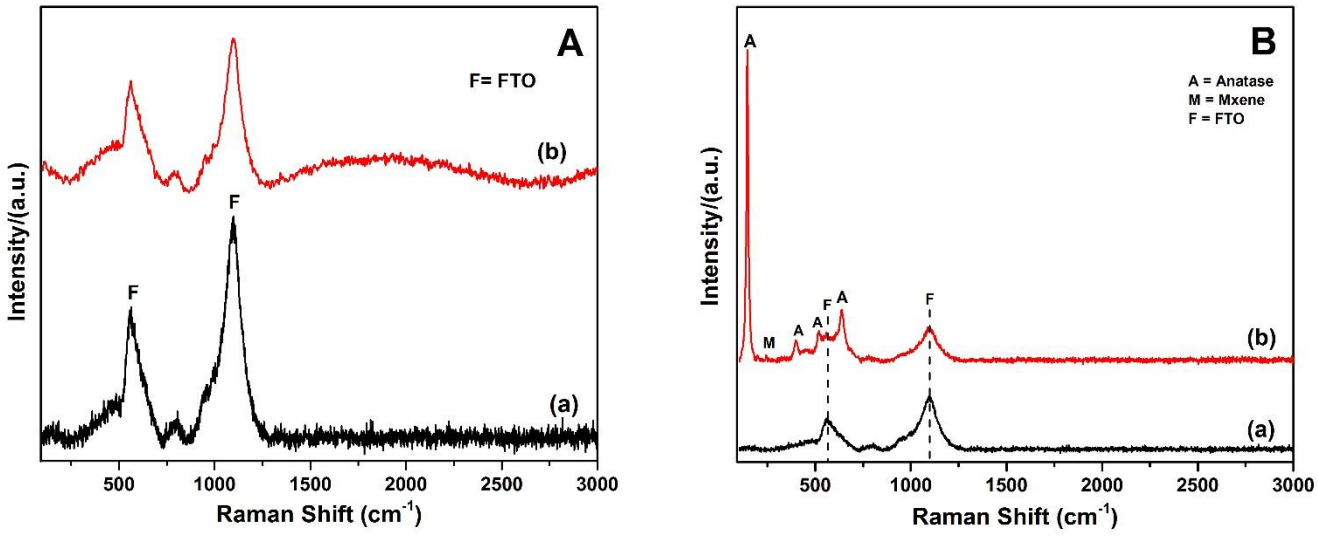

Preprints (www.preprints.org) | NOT PEER-REVIEWED | Posted: 28 September 2021 doi:10.20944/preprints202109.0459.v1

Figure 9. (A) Raman Spectra of (a) FTO, (b) Sample H; (B) Raman Spectra of (a) FTO, (b) Sample L.

The obtained structural features are further investigated by Raman spectroscopy. Figure 9A represents the Raman spectra of bare FTO (a) and Sample H: Glass/FTO/cTiO$_2$+Mx/TiCl$_4$+3%Mx/mTiO$_2$ (b) respectively. The characteristic peaks of FTO at 562 and 1094cm^{-1} [102] are greatly reduced in the deposited film. Moreover, the slightly increased intensity within the range of 1500cm^{-1} – 2500cm^{-1} in the red curve of fig 9A can be attributed to disordered graphitic carbon from Mxene contents [103]. Similar Raman results are shown in fig 9B for the synthesized film Sample L Glass/FTO/cTiO$_2$+Mx/TiCl$_4$+3%Mx/mTiO$_2$+Mx (b) and for bare FTO (a). Due to addition of Mxene in TiCl$_4$ treatment and in mesoporous layer, the Raman peaks of the anatase phases at 401, 522, and 643cm^{-1} (B1g), (A1g), and (Eg) vibrations respectively are clearly visible [104]. These results are in agreement with the XRD results above. Moreover, a small narrow peak presence at 242 is referred to in-plane (shear) modes of Ti present in Mxene [105]. Along with it, the characteristic peaks of FTO marked with F in fig 9C are highly decreased in the finally synthesized film.

Morphological analysis

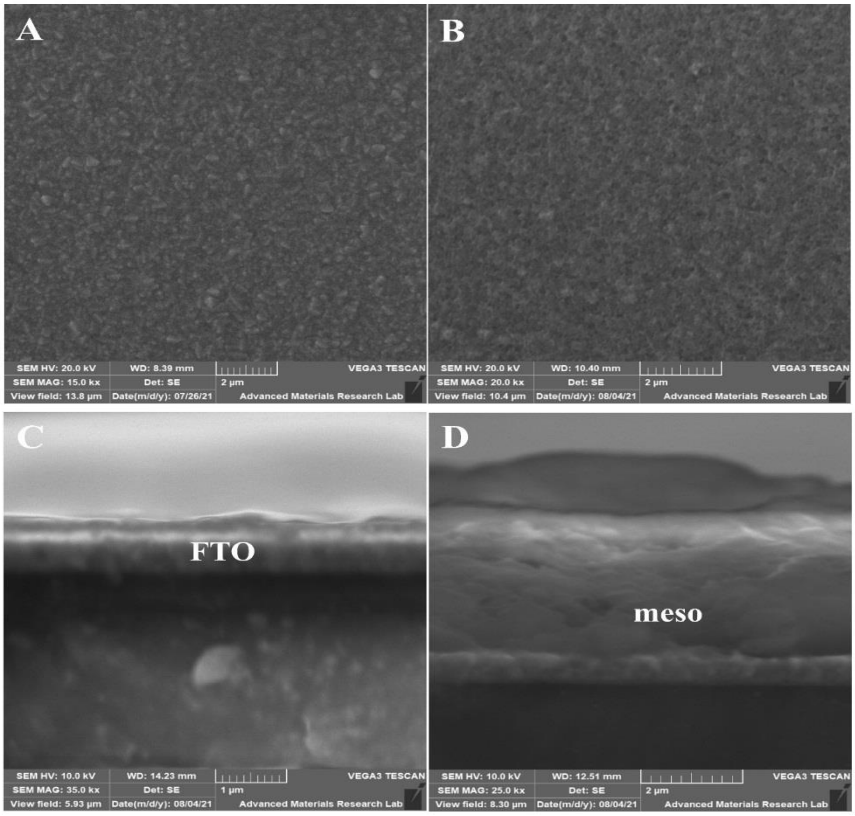

Preprints (www.preprints.org) | NOT PEER-REVIEWED | Posted: 28 September 2021 doi:10.20944/preprints202109.0459.v1

Figure 10. SEM micrographs of Front view for Sample D (A); SEM micrographs of Front view for Sample L (B); SEM micrographs of cross sectional side view of Glass/FTO (C); SEM micrographs of cross sectional top view of Sample L (D)

The morphological features of the synthesized films are analyzed through SEM micrographs shown in fig 10(A-D). The compact morphology of TiO_2:Mx without any obvious pinholes is clearly noticeable in fig 10A. The well-grown crystallites of grain size of about 0.5 µm has provided a better surface coverage. The flake like structures of Mxene sheets are clearly prominent along with spherical particles of TiO_2. Such significant interactions between Mxene flakes and TiO_2 spheres in crack-free films due to subsequent Mxene modified $TiCl_4$ treatment and post-deposition annealing are favorable for quick charge segregation [106]. The mesoporous TiO_2 layer in fig 10B is composed of ordered mesoporous structure consisting of various spherical nanograins with good porous features and an eximious interconnectivity is also present throughout the structure leading to better light harvesting efficiency (as evident from UV-Vis spectroscopy) due to their high surface area and small particle size [107]. The excellent inter-particle connectivity improves the conductance of the photogenerated electrons to the FTO contact surface [100]. The cross sectional side view of bare FTO is shown in fig 10C. Likewise the cross sectional top view of stacked architecture is composed of glass/FTO/compact TiO_2:Mx layer/mesoporous TiO_2:Mx is presented in fig 10D. The top view exhibits optimally thick mesoporous layer with slightly rough surface features. Therefore, The dense morphology of the underlying compact layer and high porosity with excellent interconnectivity of m-TiO_2 conductive scaffold are significant attributes for enhanced photovoltaic properties of the photoelectrode in terms of increased charge carrier generation at suppressed recombination rate [108].

Photo-current Measurements

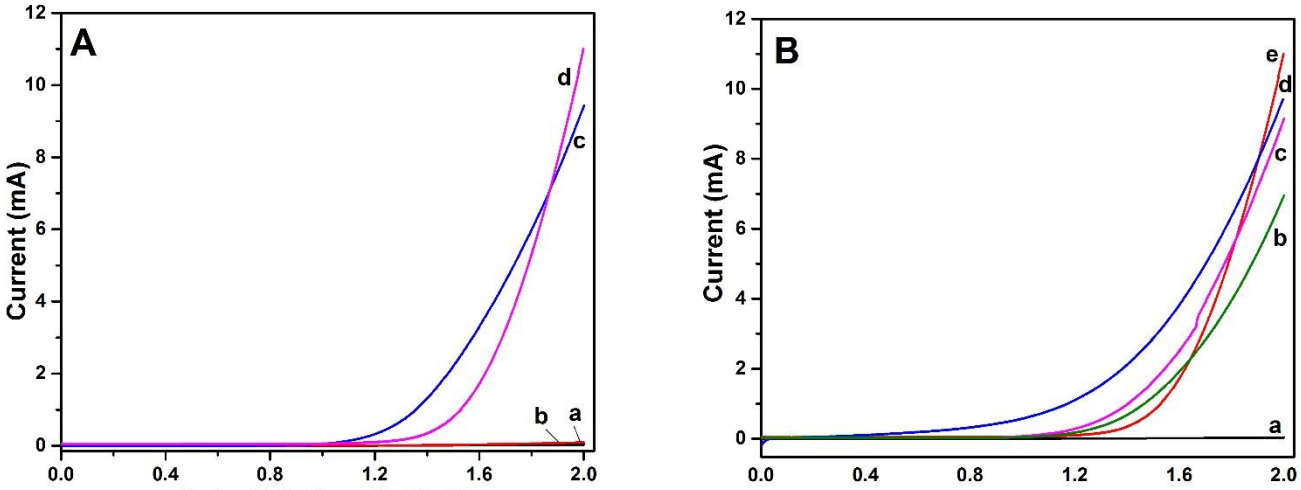

Preprints (www.preprints.org) | NOT PEER-REVIEWED | Posted: 28 September 2021 doi:10.20944/preprints202109.0459.v1

Figure 11. (A) IV curve of FTO (a) and Sample L (c) in dark, for FTO (b) Sample L (d) under illumination; (B) Phototriggered IV curve of FTO (a), Sample B (b), Sample D (c), Sample H (d), Sample L (e).

Photocurrent measurements have been studied in an electrochemical cell by varying the applied voltage between working electrode (synthesized films) and a reference electrode Hg/HgO in an aqueous 1.0M NaOH with a Pt wire as counter electrode. . Fig 12 is schematic representation of the setup. Photocurrent attributes are measured under 1 sun (100 $mWcm^{-2}$ AM 1.5) and under dark conditions displayed in fig11A. The photocurrent features of the fabricated electrodes are evaluated by linear sweep voltammetry. The scanning rate for the linear sweep voltammetry measurements are set as 20 $mV\ s^{-1}$. All the synthesized thin films are found as photoactive (presented in figure 11B) due to good crystallinity of the anatase phase. However, each films has shown different magnitudes of photocurrent depending on the material characteristics due to different Mxene contents.

Upon illuminating, the photoelectrode having highest Mxene contents in $TiCl_4$ solution as well as in mesoporous Titania (sample L) exhibited the highest photocurrent as shown in fig 11B. Two possible factors are responsible for the enhanced photocurrent: (a) better electron–hole separation due to significant interaction between Mxene and TiO_2 particles and (b) surface plasmon resonance effect of Mxene caused increased photoabsorption. Moreover, the good crystallinity in mesoporous Titania scaffold minimizes the charge annihilation process. Whereas Mxene content act as conducting medium for increased electrical conductance within mesoporous Titania network. In this study considerably high photocurrent is recorded with Mxene modified mesoporous treatment (curve e of fig 11B) in comparison with the films without mesoporous layer deposition (curve b of fig 11B). These electrical properties are supported by optical behavior of the films shown in fig 7, with considerably high absorption intensity with mesoporous Titania layer. As a consequence, greater number of absorbed photons led to increased generation of photoexcited charge carriers thus causing higher magnitude of photocurrent.

Preprints (www.preprints.org) | NOT PEER-REVIEWED | Posted: 28 September 2021 doi:10.20944/preprints202109.0459.v1

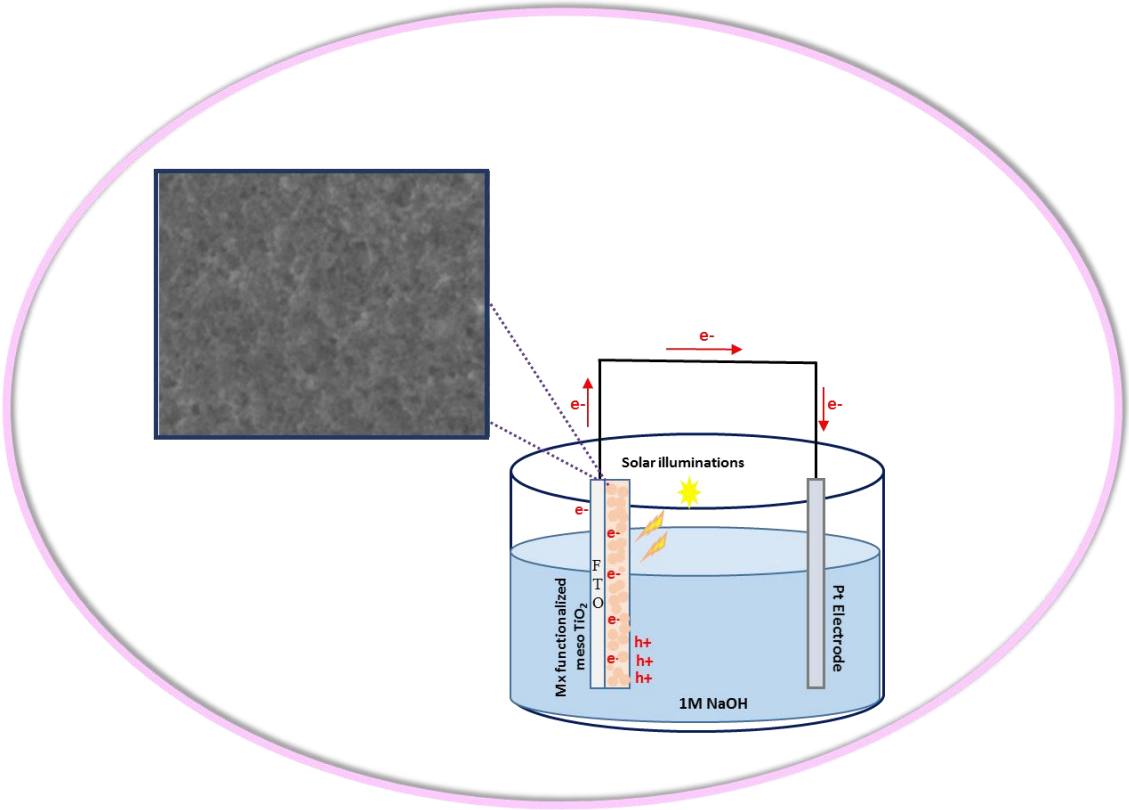

Figure 12. A pictorial view of Mxene functionalized mesoporous TiO_2 layer working as photoelectrode under light illuminations.

Conclusion

In summary, a novel combination of Mxene functionalized mesoporous TiO_2 photoelectrode is reported. The Mxene contents have been added into pristine TiO_2 through a controlled fashion in multistep spin coating process. The structural investigations reveal the increased crystallinity of anatase phase upon increased contents of Mxene in the fabricated films. Moreover, Mxene modified $TiCl_4$ treatment and post-deposition annealing conditions favor the growth of crack free films for quick charge segregation. We report enhancement of the photocurrent photo current for photoelectrodes composed of higher contents of Mxene due to the significantly improved absorption efficiency in the visible region as verified by UV–Vis absorption spectroscopy. The newly developed photoelectrodes can be further optimized by varying the amount of Mxene contents added in TiO_2 scaffold, by modulating the morphology of Mxene sheets for enhanced Opto-electric features and by adapting alternate coating procedure for large scale production such as spray pyrolysis.

Acknowledgement

Anum Iqbal acknowledges Ph.D. Assistantship (Awarded to: g00090955) for Doctoral Degree Program in Materials Science and Engineering by College of Arts & Sciences at American University of Sharjah. We would like to thank the Center for Advanced Material Research at the University of Sharjah where some of the measurements have been done.

References

[1] Y. Wang, H. Suzuki, J. Xie, O. Tomita, D.J. Martin, M. Higashi, D. Kong, R. Abe, J. Tang, Mimicking Natural Photosynthesis: Solar to Renewable H2 Fuel Synthesis by Z-Scheme Water Splitting Systems, Chemical Reviews, 118 (2018) 5201-5241.
[2] S. Zhang, C. Chen, Y. Zhou, Y. Qian, J. Ye, S. Xiong, Y. Zhao, X. Zhang, TiO2-photoanode-assisted direct-solar-energy harvesting and storage in a solar-powered redox cell using halides as active materials, ACS applied materials & interfaces, 10 (2018) 23048-23054.
[3] M.A. Green, A. Ho-Baillie, H.J. Snaith, The emergence of perovskite solar cells, Nature photonics, 8 (2014) 506-514.
[4] J.E. Thorne, S. Li, C. Du, G. Qin, D. Wang, Energetics at the surface of photoelectrodes and its influence on the photoelectrochemical properties, The journal of physical chemistry letters, 6 (2015) 4083-4088.
[5] J. Ke, F. He, H. Wu, S. Lyu, J. Liu, B. Yang, Z. Li, Q. Zhang, J. Chen, L. Lei, Nanocarbon-enhanced 2D photoelectrodes: a new paradigm in photoelectrochemical water splitting, Nano-Micro Letters, 13 (2021) 1-29.
[6] C. Acar, I. Dincer, A review and evaluation of photoelectrode coating materials and methods for photoelectrochemical hydrogen production, International Journal of Hydrogen Energy, 41 (2016) 7950-7959.
[7] Y. He, T. Hamann, D. Wang, Thin film photoelectrodes for solar water splitting, Chemical Society Reviews, 48 (2019) 2182-2215.
[8] S. Hu, N.S. Lewis, J.W. Ager, J. Yang, J.R. McKone, N.C. Strandwitz, Thin-film materials for the protection of semiconducting photoelectrodes in solar-fuel generators, The Journal of Physical Chemistry C, 119 (2015) 24201-24228.
[9] B. Moss, O. Babacan, A. Kafizas, A. Hankin, A Review of Inorganic Photoelectrode Developments and Reactor Scale-Up Challenges for Solar Hydrogen Production, Advanced Energy Materials, 11 (2021) 2003286.
[10] J.W. Yang, S.H. Ahn, H.W. Jang, Crucial role of heterostructures in highly advanced water splitting photoelectrodes, Current Opinion in Green and Sustainable Chemistry, (2021) 100454.
[11] P.J. McGinn, Thin-Film Processing Routes for Combinatorial Materials Investigations—A Review, ACS Combinatorial Science, 21 (2019) 501-515.
[12] R. Swartwout, M.T. Hoerantner, V. Bulović, Scalable Deposition Methods for Large-area Production of Perovskite Thin Films, ENERGY & ENVIRONMENTAL MATERIALS, 2 (2019) 119-145.
[13] N.-T. Nguyen, Chapter 4 - Fabrication technologies, in: N.-T. Nguyen (Ed.) Micromixers (Second Edition), William Andrew Publishing, Oxford, 2012, pp. 113-161.
[14] F. Mandoj, S. Nardis, C. Di Natale, R. Paolesse, Porphyrinoid Thin Films for Chemical Sensing, in: K. Wandelt (Ed.) Encyclopedia of Interfacial Chemistry, Elsevier, Oxford, 2018, pp. 422-443.
[15] D. Wu, C. Zhao, Y. Xu, X. Zhang, L. Yang, Y. Zhang, Z. Gao, Y.-Y. Song, Modulating Solar Energy Harvesting on TiO2 Nanochannel Membranes by Plasmonic Nanoparticle Assembly for Desalination of Contaminated Seawater, ACS Applied Nano Materials, 3 (2020) 10895-10904.

[16] W. Li, J. Liu, D. Zhao, Mesoporous materials for energy conversion and storage devices, Nature Reviews Materials, 1 (2016) 1-17.
[17] S. Guldin, S. Hüttner, P. Tiwana, M.C. Orilall, B. Ülgüt, M. Stefik, P. Docampo, M. Kolle, G. Divitini, C. Ducati, Improved conductivity in dye-sensitised solar cells through block-copolymer confined TiO 2 crystallisation, Energy & Environmental Science, 4 (2011) 225-233.
[18] D. Chen, F. Huang, Y.B. Cheng, R.A. Caruso, Mesoporous anatase TiO2 beads with high surface areas and controllable pore sizes: a superior candidate for high-performance dye-sensitized solar cells, Advanced Materials, 21 (2009) 2206-2210.
[19] J. Burschka, N. Pellet, S.-J. Moon, R. Humphry-Baker, P. Gao, M.K. Nazeeruddin, M. Grätzel, Sequential deposition as a route to high-performance perovskite-sensitized solar cells, Nature, 499 (2013) 316-319.
[20] T. Leijtens, B. Lauber, G.E. Eperon, S.D. Stranks, H.J. Snaith, The importance of perovskite pore filling in organometal mixed halide sensitized TiO2-based solar cells, The journal of physical chemistry letters, 5 (2014) 1096-1102.
[21] E.L. Unger, S.J. Fretz, B. Lim, G.Y. Margulis, M.D. McGehee, T.D.P. Stack, Sequential “click” functionalization of mesoporous titania for energy-relay dye enhanced dye-sensitized solar cells, Physical Chemistry Chemical Physics, 17 (2015) 6565-6571.
[22] L. De Marco, M. Manca, R. Buonsanti, R. Giannuzzi, F. Malara, P. Pareo, L. Martiradonna, N.M. Giancaspro, P.D. Cozzoli, G. Gigli, High-quality photoelectrodes based on shape-tailored TiO 2 nanocrystals for dye-sensitized solar cells, Journal of Materials Chemistry, 21 (2011) 13371-13379.
[23] J.H. Heo, M.S. You, M.H. Chang, W. Yin, T.K. Ahn, S.-J. Lee, S.-J. Sung, D.H. Kim, S.H. Im, Hysteresis-less mesoscopic CH3NH3PbI3 perovskite hybrid solar cells by introduction of Li-treated TiO2 electrode, Nano Energy, 15 (2015) 530-539.
[24] X. Zhang, V. Thavasi, S. Mhaisalkar, S. Ramakrishna, Novel hollow mesoporous 1D TiO2 nanofibers as photovoltaic and photocatalytic materials, Nanoscale, 4 (2012) 1707-1716.
[25] S. Reghunath, D. Pinheiro, S.D. Kr, A review of hierarchical nanostructures of TiO2: Advances and applications, Applied Surface Science Advances, 3 (2021) 100063.
[26] Y.T. Liang, B.K. Vijayan, K.A. Gray, M.C. Hersam, Minimizing Graphene Defects Enhances Titania Nanocomposite-Based Photocatalytic Reduction of CO2 for Improved Solar Fuel Production, Nano Letters, 11 (2011) 2865-2870.
[27] X. Li, Y. Bai, X. Shi, N. Su, G. Nie, R. Zhang, H. Nie, L. Ye, Applications of MXene (Ti3C2Tx) in photocatalysis: a review, Materials Advances, 2 (2021) 1570-1594.
[28] M. Naguib, O. Mashtalir, J. Carle, V. Presser, J. Lu, L. Hultman, Y. Gogotsi, M.W. Barsoum, Two-dimensional transition metal carbides, ACS nano, 6 (2012) 1322-1331.
[29] J. Halim, S. Kota, M.R. Lukatskaya, M. Naguib, M.Q. Zhao, E.J. Moon, J. Pitock, J. Nanda, S.J. May, Y. Gogotsi, Synthesis and characterization of 2D molybdenum carbide (MXene), Advanced Functional Materials, 26 (2016) 3118-3127.
[30] S. Munir, A. Rasheed, T. Rasheed, I. Ayman, S. Ajmal, A. Rehman, I. Shakir, P.O. Agboola, M.F. Warsi, Exploring the Influence of Critical Parameters for the Effective Synthesis of High-Quality 2D MXene, ACS Omega, 5 (2020) 26845-26854.
[31] C. Yang, H. Huang, H. He, L. Yang, Q. Jiang, W. Li, Recent advances in MXene-based nanoarchitectures as electrode materials for future energy generation and conversion applications, Coordination Chemistry Reviews, 435 (2021) 213806.
[32] J. Peng, X. Chen, W.-J. Ong, X. Zhao, N. Li, Surface and Heterointerface Engineering of 2D MXenes and Their Nanocomposites: Insights into Electro- and Photocatalysis, Chem, 5 (2019) 18-50.
[33] S. Jolly, M.P. Paranthaman, M. Naguib, Synthesis of Ti3C2Tz MXene from low-cost and environmentally friendly precursors, Materials Today Advances, 10 (2021) 100139.

[34] J. Ran, G. Gao, F.-T. Li, T.-Y. Ma, A. Du, S.-Z. Qiao, Ti 3 C 2 MXene co-catalyst on metal sulfide photo-absorbers for enhanced visible-light photocatalytic hydrogen production, Nature communications, 8 (2017) 1-10.
[35] S. Zhang, Y. Liu, M. Feng, B. Zhang, T. Yu, S. Xu, G. Sun, D. Wang, Leaf-like MXene nanosheets intercalated TiO2 nanorod array photoelectrode with enhanced photoelectrochemical performance, Journal of Power Sources, 484 (2021) 229236.
[36] L. He, C. Tan, C. Sheng, Y. Chen, F. Yu, Y. Chen, A β-FeOOH/MXene sandwich for high-performance anodes in lithium-ion batteries, Dalton Transactions, 49 (2020) 9268-9273.
[37] Y. Wang, Y. Li, Z. Qiu, X. Wu, P. Zhou, T. Zhou, J. Zhao, Z. Miao, J. Zhou, S. Zhuo, Fe 3 O 4@ Ti 3 C 2 MXene hybrids with ultrahigh volumetric capacity as an anode material for lithium-ion batteries, Journal of Materials Chemistry A, 6 (2018) 11189-11197.
[38] G. Zou, Z. Zhang, J. Guo, B. Liu, Q. Zhang, C. Fernandez, Q. Peng, Synthesis of MXene/Ag composites for extraordinary long cycle lifetime lithium storage at high rates, ACS applied materials & interfaces, 8 (2016) 22280-22286.
[39] C. Yang, Y. Liu, X. Sun, Y. Zhang, L. Hou, Q. Zhang, C. Yuan, In-situ construction of hierarchical accordion-like TiO2/Ti3C2 nanohybrid as anode material for lithium and sodium ion batteries, Electrochimica Acta, 271 (2018) 165-172.
[40] S.-Y. Qiu, C. Wang, Z.-X. Jiang, L.-S. Zhang, L.-L. Gu, K.-X. Wang, J. Gao, X.-D. Zhu, G. Wu, Rational design of MXene@ TiO 2 nanoarray enabling dual lithium polysulfide chemisorption towards high-performance lithium–sulfur batteries, Nanoscale, 12 (2020) 16678-16684.
[41] B.S. Yilbas, A. Al-Sharafi, H. Ali, Chapter 3 - Surfaces for Self-Cleaning, in: B.S. Yilbas, A. Al-Sharafi, H. Ali (Eds.) Self-Cleaning of Surfaces and Water Droplet Mobility, Elsevier, 2019, pp. 45-98.
[42] M. Naguib, M. Kurtoglu, V. Presser, J. Lu, J. Niu, M. Heon, L. Hultman, Y. Gogotsi, M.W. Barsoum, Two-dimensional nanocrystals produced by exfoliation of Ti3AlC2, Advanced materials, 23 (2011) 4248-4253.
[43] P. Yan, R. Zhang, J. Jia, C. Wu, A. Zhou, J. Xu, X. Zhang, Enhanced supercapacitive performance of delaminated two-dimensional titanium carbide/carbon nanotube composites in alkaline electrolyte, Journal of Power Sources, 284 (2015) 38-43.
[44] C. Zhao, Q. Wang, H. Zhang, S. Passerini, X. Qian, Two-dimensional titanium carbide/RGO composite for high-performance supercapacitors, ACS applied materials & interfaces, 8 (2016) 15661-15667.
[45] M. Ghidiu, J. Halim, S. Kota, D. Bish, Y. Gogotsi, M.W. Barsoum, Ion-exchange and cation solvation reactions in Ti3C2 MXene, Chemistry of Materials, 28 (2016) 3507-3514.
[46] Q.X. Xia, N.M. Shinde, J.M. Yun, T. Zhang, R.S. Mane, S. Mathur, K.H. Kim, Bismuth oxychloride/MXene symmetric supercapacitor with high volumetric energy density, Electrochimica Acta, 271 (2018) 351-360.
[47] C. Peng, P. Wei, X. Chen, Y. Zhang, F. Zhu, Y. Cao, H. Wang, H. Yu, F. Peng, A hydrothermal etching route to synthesis of 2D MXene (Ti3C2, Nb2C): Enhanced exfoliation and improved adsorption performance, Ceramics International, 44 (2018) 18886-18893.
[48] H. Wang, Y. Wu, J. Zhang, G. Li, H. Huang, X. Zhang, Q. Jiang, Enhancement of the electrical properties of MXene Ti3C2 nanosheets by post-treatments of alkalization and calcination, Materials Letters, 160 (2015) 537-540.
[49] X. Li, G. Fan, C. Zeng, Synthesis of ruthenium nanoparticles deposited on graphene-like transition metal carbide as an effective catalyst for the hydrolysis of sodium borohydride, International journal of hydrogen energy, 39 (2014) 14927-14934.
[50] Y. Huang, H. Yang, Y. Zhang, Y. Zhang, Y. Wu, M. Tian, P. Chen, R. Trout, Y. Ma, T.-H. Wu, Y. Wu, N. Liu, A safe and fast-charging lithium-ion battery anode using MXene supported Li3VO4, Journal of Materials Chemistry A, 7 (2019) 11250-11256.

[51] G.P. Lim, C.F. Soon, M. Morsin, M.K. Ahmad, N. Nayan, K.S. Tee, Synthesis, characterization and antifungal property of Ti3C2Tx MXene nanosheets, Ceramics International, 46 (2020) 20306-20312.
[52] C.B. Cockreham, X. Zhang, H. Li, E. Hammond-Pereira, J. Sun, S.R. Saunders, Y. Wang, H. Xu, D. Wu, Inhibition of AlF3· 3H2O Impurity Formation in Ti3C2T x MXene Synthesis under a Unique CoF x/HCl Etching Environment, ACS Applied Energy Materials, 2 (2019) 8145-8152.
[53] Y. Li, X. Zhou, J. Wang, Q. Deng, M. Li, S. Du, Y.-H. Han, J. Lee, Q. Huang, Facile preparation of in situ coated Ti 3 C 2 T x/Ni 0.5 Zn 0.5 Fe 2 O 4 composites and their electromagnetic performance, RSC Advances, 7 (2017) 24698-24708.
[54] Y. Cao, Q. Deng, Z. Liu, D. Shen, T. Wang, Q. Huang, S. Du, N. Jiang, C.-T. Lin, J. Yu, Enhanced thermal properties of poly (vinylidene fluoride) composites with ultrathin nanosheets of MXene, RSC advances, 7 (2017) 20494-20501.
[55] J.E. Spanier, S. Gupta, M. Amer, M.W. Barsoum, Vibrational behavior of the M n+ 1 A X n phases from first-order Raman scattering (M= Ti, V, Cr, A= Si, X= C, N), Physical Review B, 71 (2005) 012103.
[56] R. Syamsai, P. Kollu, S.K. Jeong, A.N. Grace, Synthesis and properties of 2D-titanium carbide MXene sheets towards electrochemical energy storage applications, Ceramics International, 43 (2017) 13119-13126.
[57] A. Sarycheva, Y. Gogotsi, Raman Spectroscopy Analysis of the Structure and Surface Chemistry of Ti3C2Tx MXene, Chemistry of Materials, 32 (2020) 3480-3488.
[58] L. Cheng, Q. Chen, J. Li, H. Liu, Boosting the photocatalytic activity of CdLa2S4 for hydrogen production using Ti3C2 MXene as a co-catalyst, Applied Catalysis B: Environmental, 267 (2020) 118379.
[59] S.A. Melchior, K. Raju, I.S. Ike, R.M. Erasmus, G. Kabongo, I. Sigalas, S.E. Iyuke, K.I. Ozoemena, High-voltage symmetric supercapacitor based on 2D titanium carbide (MXene, Ti2CTx)/carbon nanosphere composites in a neutral aqueous electrolyte, Journal of The Electrochemical Society, 165 (2018) A501.
[60] S. Lai, J. Jeon, S.K. Jang, J. Xu, Y.J. Choi, J.-H. Park, E. Hwang, S. Lee, Surface group modification and carrier transport properties of layered transition metal carbides (Ti2CTx, T:–OH,–F and–O), Nanoscale, 7 (2015) 19390-19396.
[61] F. Liu, A. Zhou, J. Chen, H. Zhang, J. Cao, L. Wang, Q. Hu, Preparation and methane adsorption of two-dimensional carbide Ti 2 C, Adsorption, 22 (2016) 915-922.
[62] J.y. Ma, M. Sun, Y.a. Zhu, H. Zhou, K. Wu, J. Xiao, M. Wu, Highly Effective 2D Layer Structured Titanium Carbide Electrode for Dye-Sensitized and Perovskite Solar Cells, ChemElectroChem, 7 (2020) 1149-1154.
[63] M. Han, X. Yin, H. Wu, Z. Hou, C. Song, X. Li, L. Zhang, L. Cheng, Ti3C2 MXenes with Modified Surface for High-Performance Electromagnetic Absorption and Shielding in the X-Band, ACS Applied Materials & Interfaces, 8 (2016) 21011-21019.
[64] A.C. Ferrari, J. Robertson, Interpretation of Raman spectra of disordered and amorphous carbon, Physical review B, 61 (2000) 14095.
[65] V. Presser, M. Naguib, L. Chaput, A. Togo, G. Hug, M.W. Barsoum, First-order Raman scattering of the MAX phases: Ti2AlN, Ti2AlC0. 5N0. 5, Ti2AlC,(Ti0. 5V0. 5) 2AlC, V2AlC, Ti3AlC2, and Ti3GeC2, Journal of Raman Spectroscopy, 43 (2012) 168-172.
[66] B. Wang, A. Zhou, F. Liu, J. Cao, L. Wang, Q. Hu, Carbon dioxide adsorption of two-dimensional carbide MXenes, Journal of Advanced Ceramics, 7 (2018) 237-245.
[67] T. Hu, J. Wang, H. Zhang, Z. Li, M. Hu, X. Wang, Vibrational properties of Ti 3 C 2 and Ti 3 C 2 T 2 (T= O, F, OH) monosheets by first-principles calculations: a comparative study, Physical Chemistry Chemical Physics, 17 (2015) 9997-10003.
[68] C.E. Shuck, A. Sarycheva, M. Anayee, A. Levitt, Y. Zhu, S. Uzun, V. Balitskiy, V. Zahorodna, O. Gogotsi, Y. Gogotsi, Scalable synthesis of Ti3C2Tx mxene, Advanced Engineering Materials, 22 (2020) 1901241.

[69] O. Kaipoldayev, Y. Mukhametkarimov, R. Nemkaeva, G. Baigarinova, M. Aitzhanov, A. Muradov, N. Guseinov, Studying of 2D titanium carbide structure by Raman spectroscopy after heat treatment in argon and hydrogen atmospheres, Eurasian Chemico-Technological Journal, 19 (2017) 197-200.
[70] R. Li, L. Zhang, L. Shi, P. Wang, MXene Ti3C2: an effective 2D light-to-heat conversion material, ACS nano, 11 (2017) 3752-3759.
[71] F. Han, S. Luo, L. Xie, J. Zhu, W. Wei, X. Chen, F. Liu, W. Chen, J. Zhao, L. Dong, Boosting the yield of MXene 2D sheets via a facile hydrothermal-assisted intercalation, ACS applied materials & interfaces, 11 (2019) 8443-8452.
[72] L. Cheng, Y. Tang, M. Xie, Y. Sun, H. Liu, 2D ultrathin NiMOF decorated by Ti3C2 MXene for highly improved photocatalytic performance, Journal of Alloys and Compounds, 864 (2021) 158913.
[73] B. Shao, J. Wang, Z. Liu, G. Zeng, L. Tang, Q. Liang, Q. He, T. Wu, Y. Liu, X. Yuan, Ti3C2Tx MXene decorated black phosphorus nanosheets with improved visible-light photocatalytic activity: experimental and theoretical studies, Journal of Materials Chemistry A, 8 (2020) 5171-5185.
[74] J. Xuan, Z. Wang, Y. Chen, D. Liang, L. Cheng, X. Yang, Z. Liu, R. Ma, T. Sasaki, F. Geng, Organic-base-driven intercalation and delamination for the production of functionalized titanium carbide nanosheets with superior photothermal therapeutic performance, Angewandte Chemie, 128 (2016) 14789-14794.
[75] Y. Xie, M.M. Rahman, S. Kareem, H. Dong, F. Qiao, W. Xiong, X. Liu, N. Li, X. Zhao, Facile synthesis of CuS/MXene nanocomposites for efficient photocatalytic hydrogen generation, CrystEngComm, 22 (2020) 2060-2066.
[76] R. Tang, S. Zhou, C. Li, R. Chen, L. Zhang, Z. Zhang, L. Yin, Janus-Structured Co-Ti3C2 MXene Quantum Dots as a Schottky Catalyst for High-Performance Photoelectrochemical Water Oxidation, Advanced Functional Materials, 30 (2020) 2000637.
[77] Q. Luo, B. Chai, M. Xu, Q. Cai, Preparation and photocatalytic activity of TiO 2-loaded Ti 3 C 2 with small interlayer spacing, Applied Physics A, 124 (2018) 1-8.
[78] K. Chaudhuri, Z. Wang, M. Alhabeb, K. Maleski, Y. Gogotsi, V. Shalaev, A. Boltasseva, Optical Properties of MXenes, in: 2D Metal Carbides and Nitrides (MXenes), Springer, 2019, pp. 327-346.
[79] A. Sarycheva, T. Makaryan, K. Maleski, E. Satheeshkumar, A. Melikyan, H. Minassian, M. Yoshimura, Y. Gogotsi, Two-dimensional titanium carbide (MXene) as surface-enhanced Raman scattering substrate, The Journal of Physical Chemistry C, 121 (2017) 19983-19988.
[80] H. Zhang, M. Li, J. Cao, Q. Tang, P. Kang, C. Zhu, M. Ma, 2D a-Fe2O3 doped Ti3C2 MXene composite with enhanced visible light photocatalytic activity for degradation of Rhodamine B, Ceramics International, 44 (2018) 19958-19962.
[81] Q. Liu, X. Tan, S. Wang, F. Ma, H. Znad, Z. Shen, L. Liu, S. Liu, MXene as a non-metal charge mediator in 2D layered CdS@ Ti3C2@ TiO2 composites with superior Z-scheme visible light-driven photocatalytic activity, Environmental Science: Nano, 6 (2019) 3158-3169.
[82] L. Yang, Y. Dall'Agnese, K. Hantanasirisakul, C.E. Shuck, K. Maleski, M. Alhabeb, G. Chen, Y. Gao, Y. Sanehira, A.K. Jena, SnO 2–Ti 3 C 2 MXene electron transport layers for perovskite solar cells, Journal of Materials Chemistry A, 7 (2019) 5635-5642.
[83] L. Yang, C. Dall'Agnese, Y. Dall'Agnese, G. Chen, Y. Gao, Y. Sanehira, A.K. Jena, X.F. Wang, Y. Gogotsi, T. Miyasaka, Surface-Modified Metallic Ti3C2Tx MXene as Electron Transport Layer for Planar Heterojunction Perovskite Solar Cells, Advanced Functional Materials, 29 (2019) 1905694.
[84] Z. Li, L. Wang, D. Sun, Y. Zhang, B. Liu, Q. Hu, A. Zhou, Synthesis and thermal stability of two-dimensional carbide MXene Ti3C2, Materials Science and Engineering: B, 191 (2015) 33-40.
[85] A. Feng, Y. Yu, Y. Wang, F. Jiang, Y. Yu, L. Mi, L. Song, Two-dimensional MXene Ti3C2 produced by exfoliation of Ti3AlC2, Materials & Design, 114 (2017) 161-166.
[86] B. Shen, Z. Hu, K. Sun, C. Lu, Y. Jiang, J. Zhang, Y. Chen, Y. Zhu, Conformal coverage of TiO2 compact layers for high-efficient planar heterojunction perovskite solar cells, Organic Electronics, 59 (2018) 177-183.

[87] D. Huh, K. Oh, M. Kim, H.-J. Choi, D.S. Kim, H. Lee, Selectively patterned TiO 2 nanorods as electron transport pathway for high performance perovskite solar cells, Nano Research, 12 (2019) 601-606.
[88] I. Dundar, A. Mere, V. Mikli, M. Krunks, I. Oja Acik, Thickness Effect on Photocatalytic Activity of TiO2 Thin Films Fabricated by Ultrasonic Spray Pyrolysis, Catalysts, 10 (2020) 1058.
[89] S. Kumar, A. Aftab, M.I. Ahmad, Compact Titania Films by Spray Pyrolysis for Application as ETL in Perovskite Solar Cells, Journal of Electronic Materials, 49 (2020) 7159-7167.
[90] C. Zhang, Y. Luo, X. Chen, W. Ou-Yang, Y. Chen, Z. Sun, S. Huang, Influence of different TiO2 blocking films on the photovoltaic performance of perovskite solar cells, Applied Surface Science, 388 (2016) 82-88.
[91] J. Qin, Z. Zhang, W. Shi, Y. Liu, H. Gao, Y. Mao, The optimum titanium precursor of fabricating TiO 2 compact layer for perovskite solar cells, Nanoscale research letters, 12 (2017) 1-9.
[92] P. Makuła, M. Pacia, W. Macyk, How To Correctly Determine the Band Gap Energy of Modified Semiconductor Photocatalysts Based on UV–Vis Spectra, The Journal of Physical Chemistry Letters, 9 (2018) 6814-6817.
[93] Z. Arshad, A.H. Khoja, S. Shakir, A. Afzal, M. Mujtaba, M.E.M. Soudagar, H. Fayaz, S. Farukh, M. Saeed, Magnesium doped TiO2 as an efficient electron transport layer in perovskite solar cells, Case Studies in Thermal Engineering, (2021) 101101.
[94] L. Yang, D. Kan, C. Dall'Agnese, Y. Dall'Agnese, B. Wang, A.K. Jena, Y. Wei, G. Chen, X.-F. Wang, Y. Gogotsi, Performance improvement of MXene-based perovskite solar cells upon property transition from metallic to semiconductive by oxidation of Ti 3 C 2 T x in air, Journal of Materials Chemistry A, 9 (2021) 5016-5025.
[95] A. Möllmann, D. Gedamu, P. Vivo, R. Frohnhoven, D. Stadler, T. Fischer, I. Ka, M. Steinhorst, R. Nechache, F. Rosei, Highly compact TiO2 films by spray pyrolysis and application in perovskite solar cells, Advanced engineering materials, 21 (2019) 1801196.
[96] Y. Lv, R. Yuan, B. Cai, B. Bahrami, A.H. Chowdhury, C. Yang, Y. Wu, Q. Qiao, S. Liu, W.H. Zhang, High-Efficiency Perovskite Solar Cells Enabled by Anatase TiO2 Nanopyramid Arrays with an Oriented Electric Field, Angewandte Chemie International Edition, 59 (2020) 11969-11976.
[97] X. Zhao, J. Zhao, J. He, B. Li, Y. Zhang, J. Hu, H. Wang, D. Zhang, Q. Liu, Porous anatase TiO2 nanocrystal derived from the metal–organic framework as electron transport material for carbon-based perovskite solar cells, ACS Applied Energy Materials, 3 (2020) 6180-6187.
[98] D. Raval, M. Jani, H. Chaliyawala, A. Joshi, I. Mukhopadhyay, A. Ray, Solar to chemical energy conversion using titania nanorod photoanodes augmented by size distribution of plasmonic Au-nanoparticle, Materials Chemistry and Physics, 231 (2019) 322-334.
[99] H. Tang, S. Zhuang, Z. Bao, C. Lao, Y. Mei, Two-step oxidation of mxene in the synthesis of layer-stacked anatase titania with enhanced lithium-storage performance, ChemElectroChem, 3 (2016) 871-876.
[100] A. Sreedhar, H. Jung, J.H. Kwon, J. Yi, Y. Sohn, J.S. Gwag, Novel composite ZnO/TiO2 thin film photoanodes for enhanced visible-light-driven photoelectrochemical water splitting activity, Journal of Electroanalytical Chemistry, 804 (2017) 92-98.
[101] R. Dubey, S. Singh, Investigation of structural and optical properties of pure and chromium doped TiO2 nanoparticles prepared by solvothermal method, Results in physics, 7 (2017) 1283-1288.
[102] Z. Jiang, D. Yang, N. Wang, F. Zhang, B. Zhao, S. Tan, J. Zhang, Inverted polymer solar cells with TiO 2 electron extraction layers prepared by magnetron sputtering, Science China Chemistry, 56 (2013) 1573-1577.
[103] M. Naguib, O. Mashtalir, M.R. Lukatskaya, B. Dyatkin, C. Zhang, V. Presser, Y. Gogotsi, M.W. Barsoum, One-step synthesis of nanocrystalline transition metal oxides on thin sheets of disordered graphitic carbon by oxidation of MXenes, Chemical communications, 50 (2014) 7420-7423.

 doi:10.20944/preprints202109.0459.v1

[104] H. Li, J. Robichaud, Y. Djaoued, A simple way to fabricate pure anatase 2D TiO 2 IO monolayer: structure, color control and its application in electrochromism, RSC Advances, 11 (2021) 8065-8072.
[105] Y.-Y. Yang, W.-T. Zhou, W.-L. Song, Q.-Q. Zhu, H.-J. Xiong, Y. Zhang, S. Cheng, P.-F. Luo, Y.-W. Lu, Terminal Groups-Dependent Near-Field Enhancement Effect of Ti 3 C 2 T x Nanosheets, Nanoscale research letters, 16 (2021) 1-7.
[106] S.R. Gajjela, K. Ananthanarayanan, C. Yap, M. Grätzel, P. Balaya, Synthesis of mesoporous titanium dioxide by soft template based approach: characterization and application in dye-sensitized solar cells, Energy & Environmental Science, 3 (2010) 838-845.
[107] N. Mozaffari, M.R. Mohammadi, Z.A. Garmaroudi, P.S.M. Gharavi, Comparative study on effect of titania morphology for light harvesting and scattering of DSSCs: Mesoporous nanoparticles, microspheres, and dandelion-like particles, Environmental Progress & Sustainable Energy, 35 (2016) 1818-1826.
[108] J.T. Park, J.H. Prosser, S.H. Ahn, S.J. Kim, J.H. Kim, D. Lee, Enhancing the Performance of Solid-State Dye-Sensitized Solar Cells Using a Mesoporous Interfacial Titania Layer with a Bragg Stack, Advanced Functional Materials, 23 (2013) 2193-2200.